nature neuroscience

Article

https://doi.org/10.1038/s41593-024-01782-5

Multimodal evaluation of network activity and optogenetic interventions in human hippocampal slices

Received: 24 August 2023

Accepted: 30 August 2024

Published online: 15 November 2024

Check for updates

John P. Andrews[1,18], Jinghui Geng[2,3,18], Kateryna Voitiuk[3,4,18], Matthew A. T. Elliott[3,4], David Shin[1], Ash Robbins[2,3], Alex Spaeth[2,3], Albert Wang[1], Lin Li[5], Daniel Solis[4], Matthew G. Keefe[1], Jessica L. Sevetson[3,6], Julio A. Rivera de Jesús[7], Kevin C. Donohue[8], H. Hanh Larson[9], Drew Ehrlich[3,10], Kurtis I. Auguste[1], Sofie Salama[3,6], Vikaas Sohal[8], Tal Sharf[4], David Haussler[2,3,4], Cathryn R. Cadwell[1,9,11], David V. Schaffer[5,7,12,13,14,15], Edward F. Chang[1,11] ✉, Mircea Teodorescu[2,3,4] ✉ & Tomasz Jan Nowakowski[1,8,11,16,17] ✉

Seizures are made up of the coordinated activity of networks of neurons, suggesting that control of neurons in the pathologic circuits of epilepsy could allow for control of the disease. Optogenetics has been effective at stopping seizure-like activity in non-human disease models by increasing inhibitory tone or decreasing excitation, although this effect has not been shown in human brain tissue. Many of the genetic means for achieving channelrhodopsin expression in non-human models are not possible in humans, and vector-mediated methods are susceptible to species-specific tropism that may affect translational potential. Here we demonstrate adeno-associated virus–mediated, optogenetic reductions in network firing rates of human hippocampal slices recorded on high-density microelectrode arrays under several hyperactivity-provoking conditions. This platform can serve to bridge the gap between human and animal studies by exploring genetic interventions on network activity in human brain tissue.

Epilepsy is a disease of aberrant neuronal activity that results from an imbalance of excitation and inhibition[1–3]. Francis Crick famously envisioned the potential of using light to precisely control neuronal populations in the human brain[4–6]. Since their discovery, light-responsive channelrhodopsins[7] have become a cornerstone of modern neuroscience studies[8,9]. Although optogenetic interventions have shown tremendous promise in non-human disease models of epilepsy[10,11], whether such tools will translate into human neural circuits, and under what conditions, remains unclear.

Although direct application of optogenetics in the human brain is not currently possible, it has been translated for use in human retina[12,13]. The use of optogenetics in research on human brain tissue has the potential to uncover key parameters for evaluating the potential efficacy of alternative therapeutic strategies. Development of any such therapies involving vector delivery of activity-modulating genes would benefit from data in a directly relevant model, namely human brain tissue.

Human brain tissue slices have been used for decades to probe mechanisms of epilepsy[14–17], and single-neuron patch-clamping data exist showing that cells transduced with an activating channelrhodopsin in human brain slice can be depolarized with light[18]. However, optogenetics has never been used to modulate network activity in a human brain slice model. Activation of inhibitory GABAergic neurons[10,19] and silencing of glutamatergic neurons[20,21] have both

A full list of affiliations appears at the end of the paper. ✉e-mail: edward.chang@ucsf.edu; mteodore@ucsc.edu; tomasz.nowakowski@ucsf.edu

https://doi.org/10.1038/s41593-024-01782-5

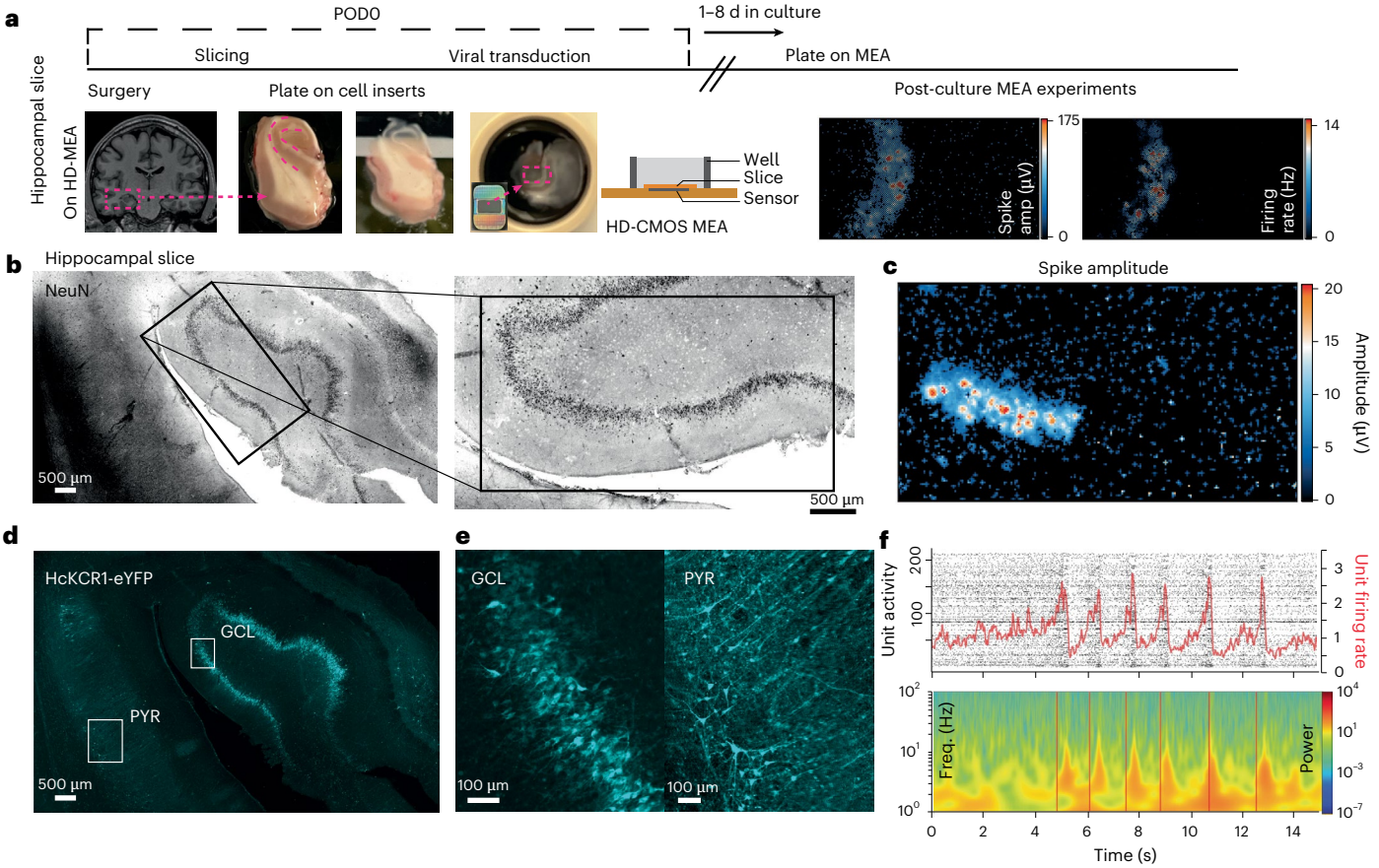

Fig. 1 | HD-MEA recordings of human hippocampal slices. a, Workflow of hippocampal slice recordings of HD-MEAs. Hippocampus specimens were collected on postoperative day 0 (POD0, day of surgery), sliced and plated on cell culture inserts. Transducing viral vectors was done on the same day as surgery. After 5–8 d in culture, slices were plated on HD-MEAs for recording experiments. **b**, NeuN staining of a slice with a black rectangle overlaying the HD-MEA recording area (left) and higher magnification of the same image with black rectangle denoting the HD-MEA recording surface (right). **c**, Activity scan showing amplitude of spike activity in the area denoted by the rectangle in **b**. **d**, Co-localization of eYFP with neuron-dense areas of the same hippocampal slice from **b** (slice 10F), one of eight slices transduced with AAV9-HcKCR1 with correlative electrophysiologic data. **e**, Left, insets of areas shown in **d**, correlating with the GCL of the dentate gyrus. Right, area of CA1 showing areas of pyramidal (PYR) cell morphology. **f**, Top, raster plot of unit activity with average unit firing rate (Hz) overlaid in red, demonstrating a sample of rhythmic bursting activity after adding KA to a hippocampal slice (slice 10F). Bottom, local field potential from select electrodes from recording above, showing discrete increases in local field potential frequency bands strongest in the theta range. Scale bars are shown in microns.

shown promise in animal models of epilepsy. Still, neither of these approaches has been demonstrated in a human brain slice model.

Despite meaningful insights into human hippocampal physiology, the vectors, genetic models and optogenetic techniques available for circuit manipulation in non-human models have far outpaced those developed for human brain slice models[21–26]. Species-specific differences present a major barrier to developing therapeutic modalities[27,28] because cross-species applicability can be unpredictable. A model for evaluating adeno-associated viruses (AAVs) in human brain slice models of human disease may provide a valuable method to screen for translational potential.

Tools for delivering genetic payloads to specific neuronal cell types in a model-agnostic way are advancing rapidly[29–33] and offer therapeutic potential[32,34,35]. For example, if AAV vectors can be combined with enhancers or promoters that selectively promote gene expression in a molecularly defined subset of cells, this would allow investigation of how optogenetic control of specific cell types could impact network activity, providing a roadmap to developing interventions that modulate epileptiform activity[22,36–38].

In the present study, we sought to validate a platform that addresses the unmet need to evaluate optogenetic interventions on network activity in human brain tissue. To this end, we evaluated the network effects of AAV-mediated optogenetic activity modulation in a human brain slice model of epileptiform activity. From the view of epilepsy as an imbalance of excitation and inhibition[1], we chose to target excitability in CAMK2A-expressing neurons. We hypothesized that inhibition of a subset of CAMK2A+ neurons can limit epileptiform activity in human hippocampal networks.

Results

Human hippocampus slice culture and neuronal transduction

To model human epileptiform activity, we established human organotypic tissue slices from hippocampus tissue (Fig. 1a) donated to research by patients with drug-refractory epilepsy. Tissues were obtained from patients both with and without hippocampal sclerosis as defined by International League Against Epilepsy (ILAE) criteria[39] (Table 1). Resected tissue was sliced to 300 μm and cultured on cell inserts at the air–liquid interface in serum-free media as previously described[16,36]. Slices were transduced (Methods) with AAV9 carrying an HcKCR1 (ref. 40) transgene driven by a CAMK2A promoter and a fluorescent tag (enhanced yellow fluorescent protein (eYFP)). Fluorescent reporter expression was observed in live imaging with an epi-fluorescent microscope by day 4–6 (transduced on day 0). On the day of experiments, the slice was plated with neuron-dense areas of interest positioned over the high-density

https://doi.org/10.1038/s41593-024-01782-5

Table 1 | Patient and slice characteristics

Pt ID	Age	Sex	ILAE HS type	Slice ID	Units	Opsin	Perturbations
A	20	M	Type 3	1A	44	N/A	None
B	44	F	Type 1	2B	36	ChR2	None
C	40	F	Type 3	3C	72	HcKCR1	None
				4C	40	ChR2	None
				5C	65	HcKCR1	bic
				6C	31	N/A	None
D	46	F	No HS	7D	80	HcKCR1	bic
				8D	13	HcKCR1	bic
E	46	F	Type 2	9E	57	HcKCR1	0-Mg +/− KA
F	52	F	Type 1	10F	351	HcKCR1	0-Mg +/− KA
G	35	M	No HS	11G	55	HcKCR1	0-Mg +/− KA
				12G	17	HcKCR1	0-Mg +/− KA

Patient and characteristics of patients undergoing anterior temporal lobectomy for refractory temporal lobe epilepsy, from whom hippocampal samples were obtained. 'Pt ID' is a patient-designated letter for identifying which slices are from which patient. Age in years and sex (F, female; M, male) are also shown. Hippocampal sclerosis is designated on a binary scale, where 'y' indicates pathologically confirmed hippocampal sclerosis, and 'n' indicates no pathologically confirmed hippocampal sclerosis. 'Slice ID' uses the letter Pt ID designation combined with a numerical identifier of separate slices. A different number with the same paired letter in Slice ID designates that a slice was derived from the same patient. 'Units' refers to the maximum number of individual units recorded during experimental recordings after spike sorting and curation. 'Opsin' designates whether HcKCR1 or ChR2 was the channelrhodopsin transduced, and 'N/A' indicates no channelrhodopsin transduced. 'Perturbations' refers changes to recording media used in experiments with the designated slice. 0-Mg +/− KA, zero magnesium media with and without addition of kainic acid; bic, bicuculline; HS, hippocampal sclerosis; ILAE HS, International League Against Epilepsy classification of hippocampal sclerosis.

Table 2 | Transduction rate and units responding to optogenetic activation

Slice ID	Transduction %	≥25% FR decrease	≥50% FR decrease	≥75% FR decrease	≥90% FR decrease
3C	45	83%	81%	70%	65%
5C	36	96%	93%	86%	72%
7D	12	82%	66%	49%	36%
8D	19	100%	100%	100%	100%
9E	24	56%	51%	44%	40%
10F	54	39%	23%	13%	8%
11G	22	47%	39%	28%	15%
12G	10	46%	46%	44%	40%

'Transduction %' indicates percent of NeuN-expressing neurons co-expressing HcKCR1–eYFP in immunohistochemistry where transduction rates are calculated in areas approximating the area of slice over the recording array. %FR decrease where each column represents the percent of recorded neurons whose firing rate was reduced by ≥25%, ≥50%, ≥75% and ≥90% compared to the 10-s mean firing rate before light-ON conditions shown in Fig. 3 and Extended Data Figs. 5–7. The value in each column is the percentage of recorded units with a percent decrease by ≥ the threshold designated by the column header. FR, firing rate.

microelectrode array (HD-MEA) recording surface (Fig. 1b). A scan of the recording area electrodes was performed immediately after plating the slice to observe areas of spontaneous activity (Fig. 1c). After experiments, slices were fixed, and reporter expression was confirmed by immunohistochemistry (Fig. 1d and Extended Data Fig. 1). Reporter expression was enriched in neurons of the granule cell layer and the dentate gyrus as well as pyramidal cells (Fig. 1e and Extended Data Fig. 1). The proportion of neurons expressing eYFP in areas of high transduction ranged from 10% to 54% (Table 2). This variability may be the result of focal micropipette injection. Slices that did not show detectable eYFP were excluded from the analysis of transduction rates (Methods). Together, these results indicate that we established organotypic tissue slice cultures of the human hippocampus and reproducibly delivered genetic payloads into hippocampal CAMK2A+ neurons using a combination of AAV9 and a CAMK2A promoter-driven transcript.

Optogenetic control of human hippocampal network

HcKCR1 encodes a kalium channelrhodopsin—a potassium-selective, light-sensitive ion channel that hyperpolarizes the neuronal membrane, thus reducing the probability of spiking when activated by 530-nm light[40,41]. Unlike a more traditional Channelrhodopsin-2 (ChR2), which encodes a sodium-selective ion channel, inhibitory channelrhodopsins have never been applied to human tissue. To confirm that HcKCR1 illumination drives membrane hyperpolarization, we conducted intracellular voltage-clamp recordings. Consistent with our expectations, HcKCR1 activation resulted in hyperpolarizing currents in human hippocampal neurons (Extended Data Fig. 2). To assess whether AAV-based transduction of human neurons with optogenetic constructs is specific to HcKCR1, we transduced additional slices with an excitatory channelrhodopsin (AAV9–CAMK2A–ChR2–eYFP) packaged in the same viral vector. In this case, we observed similar extent of expression, suggesting that our methods are not limited to HcKCR1 (Extended Data Fig. 1). Together, these results demonstrate the feasibility of applying inhibitory optogenetics to human neurons.

Computational modeling of excitatory neuron inhibition

Relative rarity of human hippocampal tissue samples and the limited viability of slices can impede optimization of any step in an experimental protocol that directs testing of human tissue. Computational modeling of cellular circuits is free from these limitations. We conducted in silico modeling of hippocampal epileptiform activity based on prior electrophysiological data[42] to computationally predict the degree to which HcKCR1 activation might dampen epileptiform activity across a range of transduction rates in human neurons. The model contains dentate gyrus granule cells (GCs) providing excitatory input and basket cells (BCs) providing inhibitory input. In the model, the light-sensitive channel is modeled after the single-cell characterization of HcKCR1 (ref. 40). We varied the proportion of GCs expressing this channel to model the potential effects of variability in expression levels (Extended Data Fig. 3). In silico epileptiform activity could be dampened with optogenetic control of less than 50% of the GC population (Extended Data Fig. 3). Even at the lower limits of effective expression, the length and intensity of seizure-like events are experimentally controllable in our model (Extended Data Fig. 3). This analysis suggests that even incomplete delivery of HcKCR1 into excitatory hippocampal neurons may be sufficient to modulate network-level epileptiform activity.

HD-MEA integration with optogenetic activation

To test the effects of optically activating channelrhodopsins in our slice model, we integrated the HD-MEA recording system with fiber-coupled LED drivers to illuminate organotypic slices plated on the recording array. The associated hardware is small enough to be contained entirely in a tissue culture incubator (Fig. 2, Supplementary Fig. 1 and Supplementary Table 1). While closed in the incubator, the system is controllable from external computers. Custom software was created to allow for real-time analysis of spike event data, allowing for observation of electrophysiological activity and the impact of optogenetic perturbations with minimal delay. The system allows software control of light intensity, duration, frequency and off-time.

Optical HcKCR1-mediated inhibition of network activity

HcKCR1 activation suppressed activity in human hippocampal neurons across all experimental conditions of spontaneous and provoked activity (Fig. 3 and Table 2). Illumination with 530-nm light[40] resulted in rapid silencing of hippocampal activity (Fig. 3 and Extended

https://doi.org/10.1038/s41593-024-01782-5

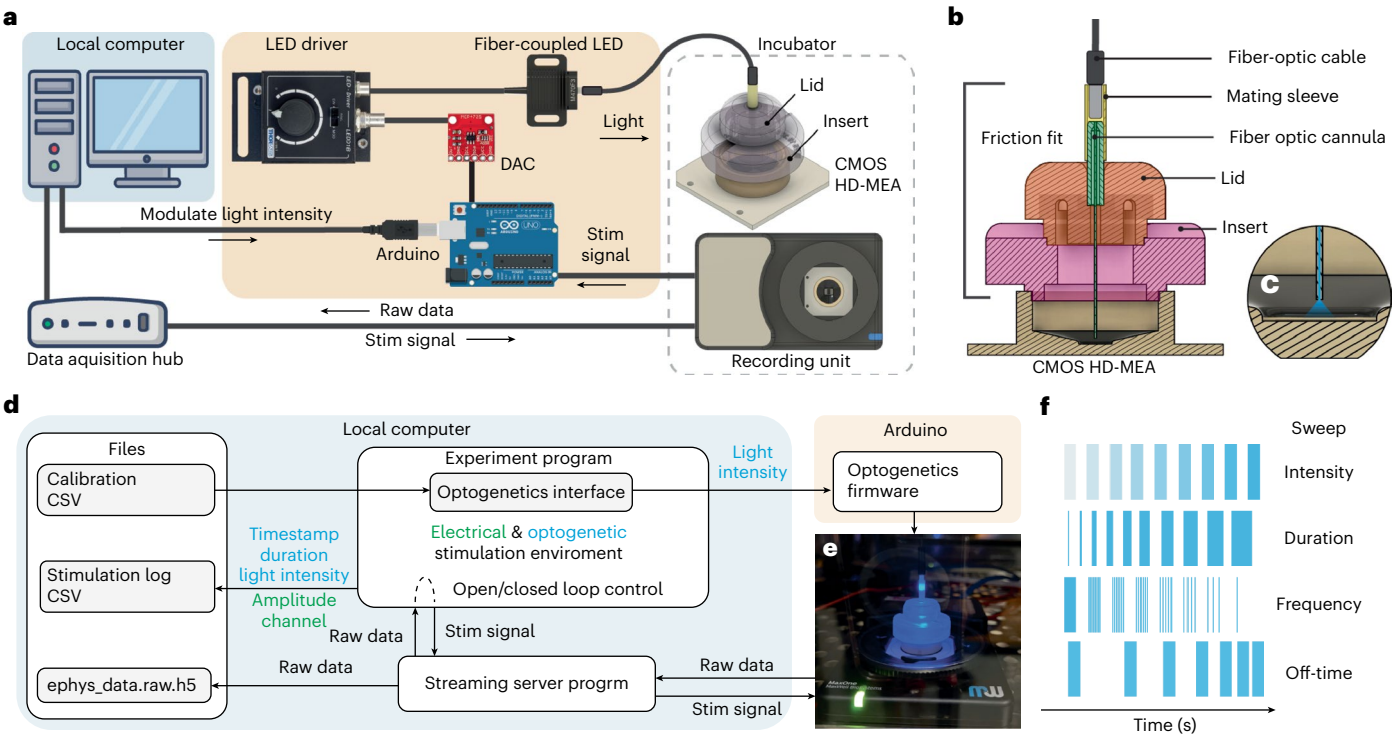

Fig. 2 | Optogenetic device for MEA. a, Hardware components: the MaxWell CMOS HD-MEA system is augmented with an optogenetic platform, consisting of an Arduino with a DAC controlling an LED driver to modulate light timing and intensity delivered to the biological sample on the HD-MEA. The optogenetic platform uses off-the-shelf optoelectronic equipment and 3D printable components (the lid and insert) for reproducibility. The MaxWell natively supports electrical stimulation. **b**, Cross-section of optogenetic well insert showing main components. **c**, Close-up of the optical fiber creating illumination. **d**, Software modules: code and data flow supporting optogenetic and electrical stimulation wrapped into Python libraries. Additional files store calibration for the expected LED power outputs, a log of stimulations delivered during an experiment with respective parameters and MaxWell voltage recording data. Cyan elements are specific to optogenetic stimulation. Green elements are specific for electrical stimulation. All other software elements are shared. **e**, Experimental setup inside the incubator showing the MaxWell chip with the optogenetic insert during an optical stimulation event. **f**, Configurable stimulation templates are part of the software modules.

Data Figs. 4–6). Constant illumination for 10 s reduces spontaneous firing rates (Fig. 3a). Changes in spike amplitude were less consistent (Extended Data Fig. 4 and Supplementary Table 2). The reduction in neuronal spiking was consistent and evident in raw data (Fig. 3a, Supplementary Video 1, Extended Data Fig. 4 and Supplementary Table 2).

Intensity scans across the full range of light intensity produced by the LED driver were carried out to determine the dynamic range of the control of neuronal firing rates as a function of illumination power (Extended Data Fig. 7). The intensity threshold was typically between (26.2 mW mm^{-2} and 31.2 mW mm^{-2}), correlating to 40–50% of the possible output from our drivers. For experiments, we used one step above the minimum threshold (that is, 50–60% intensity, translating to 31.2–35.8 mW mm^{-2}).

Decreases in neuronal firing rates during HcKCR1 optogenetic activation were obtained from $n = 8$ ex vivo hippocampal slices (Table 2 and Extended Data Figs. 4–6). We additionally carried out recordings in a hippocampal slice transduced with an identical AAV vector driving ChR2 expression (AAV9–CAMK2A–ChR2–eYFP), which demonstrated an increase in unit activity with 470-nm light illumination (Extended Data Fig. 8). This result confirms that the specificity of light-mediated change in neuronal activity is determined by the channelrhodopsin-specific physiology and not an artifact of light illumination.

AAV mediated HcKCR1 expression is sufficient to enable optogenetic modulation of network-wide spontaneous activity despite incomplete transduction (Table 2). Spontaneous activity arises from networks perched in a balanced regime that is prone to neither silence nor saturation[43]. As a result, relatively small increases in inhibitory tone at a cellular level may be insufficient to offset the imbalance necessary to generate epileptiform activity at a network level.

Optogenetic suppression in provoked hyperexcitability

Next, we tested HcKCR1-mediated optical inhibition in the context of hyperexcitable conditions. Under all these conditions, HcKCR1 activation reduced firing rates in large portions of units recorded (Table 2).

We used magnesium-free (0-Mg) media, a long-standing approach used to increase neuronal excitability and induce epileptiform activity in hippocampal preparations[14,44,45]. Clear, spontaneous bursts of activity were observed in two of four slices bathed with 0-Mg media (Fig. 3c, Extended Data Figs. 5 and 9 and Supplementary Table 3). These bursts of activity were less than 1 s in duration and several minutes apart, reminiscent of interictal epileptiform spikes[46]. During LED light illumination of slices bathed in 0-Mg media, mean firing rates were reduced compared to the rates in the absence of light illumination, although not all units responded uniformly. As an example of this spectrum of unit response, average firing rate reduction of the grouped unit activity in two slices did not meet statistical significance in the 0-Mg media conditions (Extended Data Fig. 5 and Supplementary Table 3). On a unit-level analysis, however (and evident in raster plots of Extended Data Fig. 5g,j), 15–40% of units in these slices had a decrease in firing rate of at least 90% during light-ON conditions (Table 2, 11G and 12G), demonstrating that not all units in each slice respond uniformly. Spike events during 0-Mg recording conditions were not completely absent during optical inhibition of two separate slices (Fig. 3c, t10, and Extended Data Fig. 5d,g). The spikes were far enough apart in time to prevent strong conclusions about the effects of optical inhibition on these events (Extended Data Fig. 9).

Addition of kainic acid (KA) has been used in various epilepsy models[22,47–49]. Based on other groups reporting the effectiveness of

combining multiple pro-convulsant pharmacologic interventions to induce epileptiform activity[22,50], we tested whether adding kainate to 0-Mg bathed slices would lead to epileptiform activity. The addition of KA resulted in acute elevations in firing rate, and, in two of four slices recorded with KA, rhythmic bursts of activity occurred (Fig. 3d and Extended Data Fig. 6d,g). Slices exhibiting this rhythmic bursting of unit activity also showed increased coherence across frequency power bands, most clearly in the theta band (Fig. 3f,g). Repeated 10-s periods of illumination reduced firing rates during light-ON conditions (Fig. 3d), but a causal effect of illumination on the coordinated bursts is less clear in the absence of more comprehensive characterization of the typical effects and expected frequency of rhythmic bursting with addition of KA (Extended Data Fig. 6 and Supplementary Table 4).

To explore this platform's ability to perform closed-loop illumination, we used a $GABA_AR$ blockade via the application of bicuculline to elevate firing rates above their baseline levels (Fig. 3j,k). We used the reproducible increases in firing rate with $GABA_AR$ blockade to detect and disrupt elevations in network firing. We used an automated, real-time spike event detection algorithm to trigger LED illumination when a firing rate threshold is crossed (Fig. 3h–k). The closed-loop illumination software is user-activated after bicuculline application, and when firing rates surpass a predefined threshold, it triggers 10 s of continuous illumination. This markedly reduced the firing of recorded units (Fig. 3h–k and Supplementary Video 2). This was replicated in $n = 3$ HcKCR1-expressing slices derived from $n = 2$ patients. These results demonstrate a potential benefit of optogenetic interventions in epilepsy: modulation of brain activity restricted precisely to time and anatomy in which pathologic elevations in neuronal firing occur.

In these three distinct methods of provoking a hyperexcitable state (0-Mg, 0-Mg + KA and $GABA_AR$ blockade), HcKCR1 activation in a subset of CAMK2A-expressing neurons reduced network firing rates. Fraction of neurons transduced in a recording area did not completely explain different fractions of neurons exhibiting reduced firing rates in light-ON conditions (Table 2 and Supplementary Fig. 2). The magnitude of firing rate reductions in 0-Mg and 0-Mg + KA conditions was less than that observed in physiologic media and GABAergic blockade (Supplementary Fig. 3). Although several variables may contribute to this, HcKCR1-mediated inhibition of pre-synaptic CAMK2A-expressing neurons may be partially offset by post-synaptic glutamatergic receptor activation in 0-Mg and 0-Mg + KA conditions. Whether HcKCR1 activation of CAMK2A-expressing neurons effectively interrupts provoked coherence seen in 0-Mg + KA conditions will require additional experiments to thoroughly characterize the effects of the rhythmic burst activity induced with 0-Mg + KA.

Propagation of epileptiform activity

Spatially resolved recordings of neural activity enabled by the HD-MEA allowed us to analyze signal propagation patterns over the hippocampal areas recorded during epileptiform spikes and optogenetic activation of HcKCR1. First, we examined increases in single-unit firing rates during the 0-Mg + KA spike events that make up the rhythmic bursting in the slice with the densest coverage of the granule cell layer (GCL). Plotting the units with relative increases of >3 s.d. above their baseline firing before the spike event suggested a progression from the hilar aspect of the GCL to the outer aspect (Fig. 4a–c). Owing to the theta phase coherence observed at a network level during these bursts of activity (Fig. 3f–h), we examined the spatial changes in phase coherence over time during these rhythmic bursts. Plotting the relative change in the theta phase during these bursts of activity revealed clear propagation of theta waves from the hilar aspect to the outer aspect of the GCL (Fig. 4d and Supplementary Video 3). A similar pattern of theta propagation was also observed in the rhythmic bursting during 0-Mg + KA in a separate slice, also with GCL coverage, from a different patient (Supplementary Video 4).

In one slice, there was no overlap of these rhythmic bursts during light-ON conditions (Extended Data Fig. 6g), whereas, in the other slice, these bursts did indeed have some overlap with the light-ON conditions (Figs. 3d, t6–t8). This variability suggests that reductions in overall firing rate, or reductions in $CAMK2A^+$ neuronal firing, may not always be sufficient for disrupting network coherence characteristic of epileptic circuits.

The traveling wave phenotype that we observed has never, to our knowledge, been visualized at this level of resolution. Such a granular picture of network synchronization may offer a proxy for epileptiform activity that has been unmeasurable without HD-MEA technology. These traveling waves of theta coherence during 0-Mg + KA may offer targets for evaluating the efficacy of experimental interventions.

Waveform and opto-response clustering

Reduced unit firing with HcKCR1 activation was not uniform across recorded units (Fig. 3 and Extended Data Fig. 4–6), ranging from complete silencing to more subtle or no apparent firing rate changes in other units. Given that AAV9 transduction was not uniform across the tissue, this may partially explain such a spectrum of response, but there was not a clear correlation between transduction rate and fractions of units with reduced firing (Supplementary Fig. 2). However, cell type is another variable that could affect a unit's response to HcKCR1 activation even in the presence of similar transduction. To investigate whether response parameters of the units are uniform[40,51], we investigated whether unit cell type differences could be inferred from the HD-MEA extracellular recordings.

We applied a waveform clustering method[52,53] (Methods) to group units based on features extracted from the extracellular action potential waveform (Fig. 5). This analysis yielded 12 separate clusters (Fig. 5). To validate whether the distribution of putative cell types identified by waveform clustering is consistent with anatomy, we aligned recording array electrodes with histology to approximate the anatomic slice area from which each electrode records. If waveform clusters correlate with putative cell types, then recordings over an anatomic area with a relatively homogenous cell type should be enriched for waveform clusters underrepresented in anatomic areas without such cells. We

Fig. 3 | Optogenetic inhibition of human hippocampal activity. a, Stacked raster plot of single-unit activity from a hippocampal slice expressing HcKCR1. On the *y* axis are five trials (t1–t5) of continuous 10-s illumination, stacked to line up the phase immediately preceding illumination (pre), the light-ON phase (green) and the 10 s following the end of illumination (OFF). The average firing rate of all units is overlaid (red). **b**, Heat maps of the electrode arrays showing 5-rms spike activity across the electrode recording surface during the 10-s bins shown in **a** (both **a** and **b** are from slice 3C). Black represents HcKCR1–eYFP staining. **c**, Similar stacked raster plot with firing rate overlay of a single slice recorded in 0-Mg media, followed by **d**, recordings after addition of KA to the slice (**c**–**h** are from slice 10F). **e**, Expanded picture of one of the series of rhythmic bursts of activity seen in the stacked raster of **d**. **f**, Local field potential frequency spectrum over time from a selected unit during the **e** time period. **g**, Expanded region of **e**, showing non-random coherence (see KLD in Methods) in the theta frequency band (pink) with firing rate (red) overlaid. **h**, Rose plots (on a 2-pi radian phase circle) showing non-random phase distribution of theta coherence in subsets of the highlighted burst of coordinated activity in **g(I)**. **i**, Random theta phase distribution in **g(II)**. **j**, Stacked raster of a slice showing optogenetic inhibition of activity after GABAergic blockade with bicuculline (**j** and **k** are from slice 5C). **k**, Heat maps of the electrode arrays showing 5-rms spike activity across the electrode recording surface during the 10-s bins shown in **j**. Black represents HcKCR1–eYFP staining. **l**, Schematic of closed-loop, responsive optogenetic illumination. **m**, Example of using closed-loop optogenetic silencing of bicuculline-provoked activity. Shaded red outline of red firing rate line in **a**, **c**, **d** and **j** represents standard error of the mean of firing rate. fr, firing rate.

https://doi.org/10.1038/s41593-024-01782-5

analyzed waveform clustering in areas of the dentate gyrus GCL versus recordings without GCL representation. We compared the distribution of unit waveform clusters in three slices with clear GCL coverage to six slices recorded where active recording electrodes did not overlap with GCL. Five waveform clusters were significantly overrepresented in the GCL recordings (Fig. 5 and Supplementary Table 5).

Next, to characterize the heterogeneity of unit responses to optogenetic activation, we used an HDBSCAN-based clustering

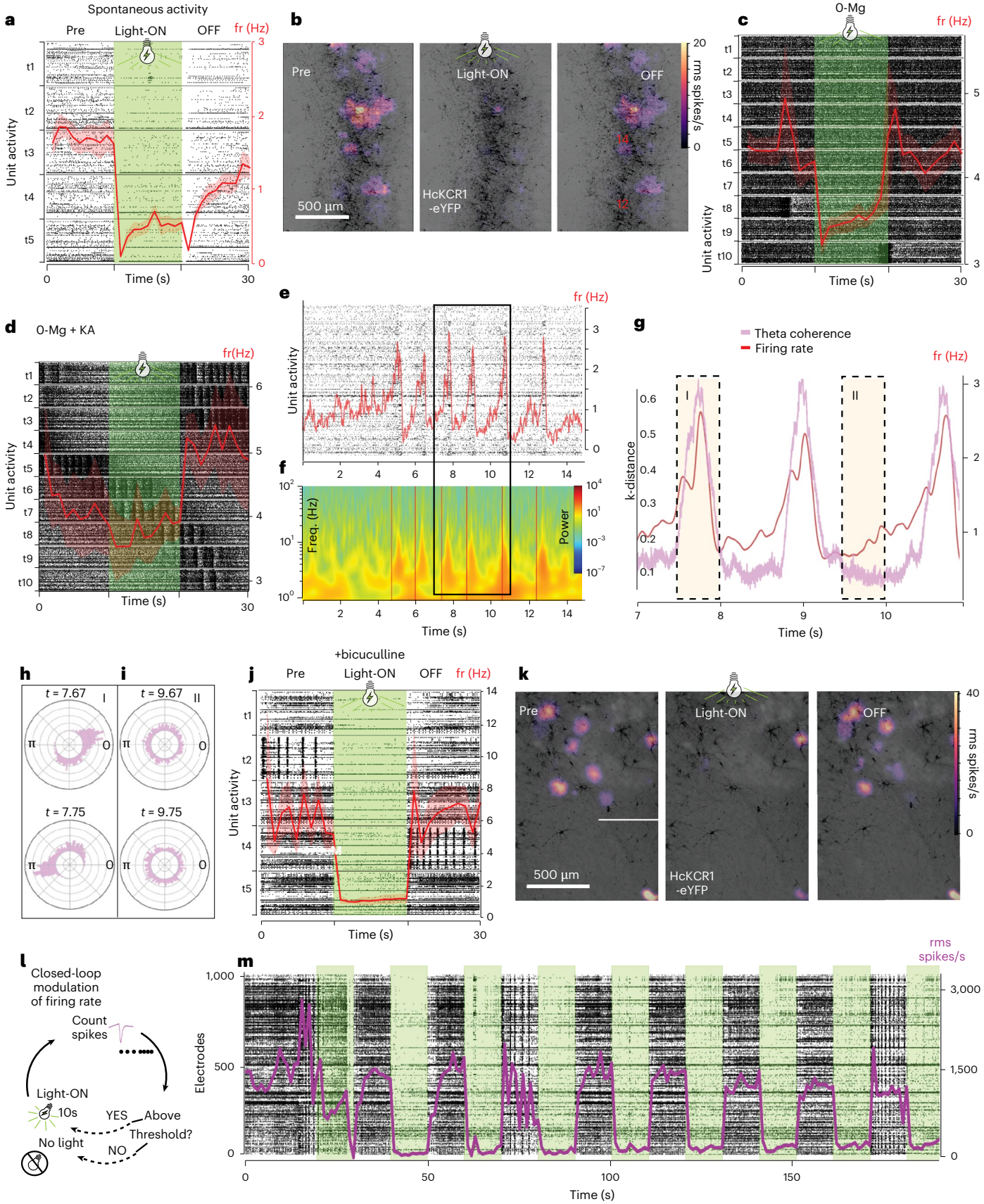

https://doi.org/10.1038/s41593-024-01782-5

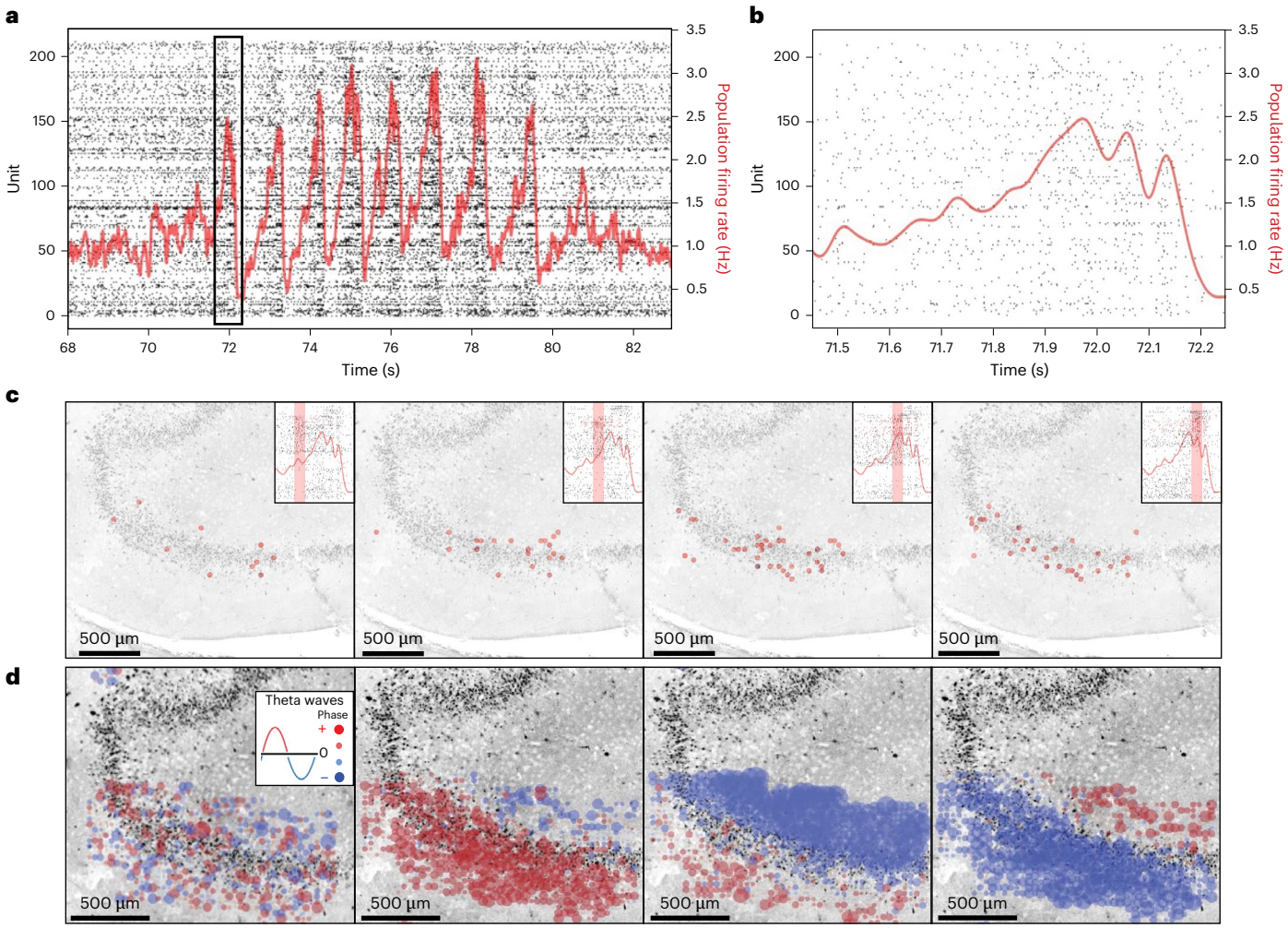

Fig. 4 | Propagation of activity over the GCL of the dentate gyrus. a, Example of rhythmic bursting activity seen in 0-Mg + KA conditions (slice 10F). **b**, Expanded raster plot with average unit activity overlaid in red of single burst of activity from the black rectangle in **a**. **c**, Sequential periods of time over the course of the single burst of unit activity seen in **b**, with red dots showing position of electrodes where units had a relative increase in firing of >3 s.d. compared to a non-bursting time period as baseline. **d**, Theta wave phase propagation from local field potential in sequential time periods for the same spike burst analyzed in **b** and **c** (Methods and Supplementary Videos 3 and 4). Red and blue represent opposite phases of the theta wave, with size of dots representing the magnitude of the phase relative to zero.

technique[54,55] (Methods). We analyzed peristimulus histograms of neuronal firing rate spanning time segments before and during optogenetic activation. We found five distinct opto-response clusters (Fig. 6a,b), four of which showed statistically significant reductions in mean firing rate and firing rate distribution with optogenetic activation (Fig. 6c).

Because our waveform clustering suggested that five of the waveform clusters were associated with recordings of the GCL, we treated these waveform clusters as a single category when testing whether opto-response clusters were associated with any putative cell types from waveform clustering. There was indeed a significant association between the GCL waveform cluster and the opto-response cluster 3 (Supplementary Table 6), in addition to associations between several other waveform and opto-response clusters. Although this is far from definitive for stipulating cell type to be the only or most prominent factor in neuronal response to HcKCR1 activation, it is consistent with the hypothesis that response to optogenetic activation may differ between cell types. Moreover, it suggests the need for further clarification of how optogenetic interventions in different cell types may affect those cell types and networks differently.

Discussion

We describe an approach for using human organotypic brain tissue as an experimental research platform for optimizing approaches to modulate neural activity at the network level in human hippocampus. Building on advances in culture techniques for maintaining viable human organotypic brain slices ex vivo, we evaluated the effectiveness of AAV-mediated delivery of inhibitory channelrhodopsins expressed in a subset of CAMK2A+ neurons to exert network-level effects in hyperexcitable conditions. By integrating HD-MEA recordings with a custom system for optogenetic control, our experiments demonstrate a robust platform for high-resolution analysis of network activity and cell-type-specific optogenetic manipulation in human hippocampus.

Optogenetics enables high spatiotemporal control over neural activity. Targeting local circuits has been shown to decrease epileptiform activity in non-human model systems[10,11,20,21,56], but application of optogenetics to human neurons has been limited. Two studies used patch-clamp recordings from single neurons to show excitatory optogenetic control of human neurons at a single-cell level[18,36]. Hyperpolarizing, potassium-specific, kalium channelrhodopsins are a new tool in the optogenetic armamentarium[40,41]. Their inhibiting effects

https://doi.org/10.1038/s41593-024-01782-5

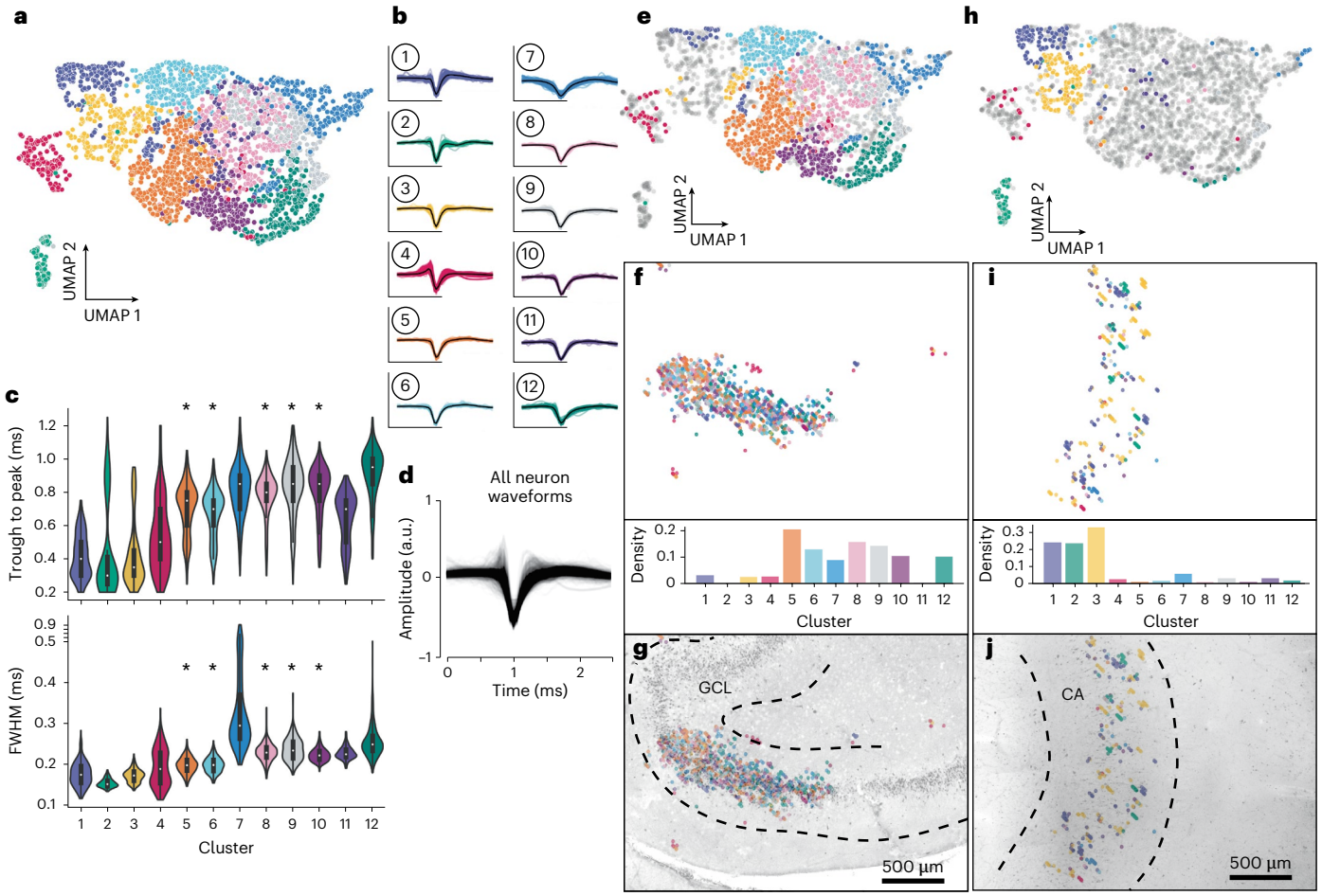

Fig. 5 | Waveform clustering. a, UMAP of waveform clusters of HD-MEA extracellular unit activity recorded from all units in slices named in Table 2. **b**, Average waveform of each cluster (black) overlaid on colored traces of all waveforms in each category. **c**, Average trough-to-peak (top) and full width at half maximum (FWHM) (bottom) features for each of the waveform clusters. For box and whisker plots, the box extends from the first quartile to the third quartile of the data, with a line at the median. The whiskers extend from the box to the farthest data point lying within 1.5× the interquartile range from the box. To determine whether clusters were significantly associated with areas of GCL coverage, neuronal units were dichotomized as being recorded from GCL on histology or not, and logistic regression (Methods) was used to estimate the odds ratio (OR) of GCL localization for units in each cluster of $n = 12$ clusters. * Comparisons were significant if $P < 0.05$ after correction for multiple comparisons (cluster 5 OR = 10.2, 95% confidence interval (CI): 5.8–18.3, $P = 2.67 \times 10^{-15}$; cluster 6 OR = 8.3, 95% CI: 4.4–15.7, $P = 1.24 \times 10^{-10}$; cluster 8 OR = 8.4, 95% CI: 4.6–15.3, $P = 5.95 \times 10^{-12}$; cluster 9 OR = 2.3, 95% CI: 1.5–3.5, $P = 7.781 \times 10^{-5}$; cluster 10 OR = 2.3, 95% CI: 1.5–3.7, $P = 3.634 \times 10^{-4}$). **d**, Overlay of all waveforms analyzed. **e**, UMAP from **a**, with units represented by slice 10F, consisting of GCL coverage, colored by waveform cluster. **f**, Units from 10F projected spatially onto the MEA recording area. Density histograms below represent the fraction of units recorded in the slice that were assigned to each waveform cluster. **g**, Units and recording area from **f** overlaid onto histology of the slice, showing GCL anatomic correlation. **h**–**j**, Same parameters as **e**–**g**, except for slice 3C, depicting with a Cornu Ammonis (CA) 1 area, with no GCL coverage. Waveform cluster association with GCL statistics is reported in Supplementary Table 5.

may be relevant to diseases of neuronal hyperactivity, such as epilepsy. This study demonstrates that optogenetic inhibition of human neurons can be used to modulate network-wide neuronal activity in human hippocampal slices.

The effects of optogenetic inhibition ofCAMK2A$^+$ neurons on network firing rates were more pronounced in the conditions of physiologic media and $GABA_AR$ blockade compared to low Mg or KA (Supplementary Fig. 3). Notably, the latter two conditions promote glutamate receptor activation. Optogenetic firing rate reductions in physiologic media and $GABA_AR$ blockade may be due to combined changes from HcKCR1-mediated inhibition of excitatory neurons as well as indirect reductions in activity of their downstream neurons. In contrast, if low Mg[17] and KA[57] promote direct activation of glutamate receptors, the downstream effects of reducing spike activity in CAMK2A$^+$ HcKCR1-expressing neurons may be less pronounced. This may also explain some persistence of epileptiform bursts during slice illumination with KA media.

In our preparations, adding KA to slices in low-Mg media resulted in rhythmic bursting events, consistent with previous studies[22]. This bursting activity appeared to be less common during optogenetic activation of HcKCR1, with none occurring during light-ON conditions in slice 11G (Extended Data Fig. 6g) and less common, but still present, during three of 10 trials in slice 10F (Extended Data Fig. 6d). Incomplete silencing is not explained by transduction rate in these slices (Supplementary Fig. 2). This may also be related to the increased exogenous glutamatergic activation by KA conditions discussed above. Further characterization of the rhythmic bursting observed is needed to understand effective methods for targeting this electrophysiologic phenotype. Interestingly, the observed results show remarkable similarity to in silico modeling (Extended Data Fig. 3), where coordinated activity was reduced in magnitude and frequency (but not completely extinguished) compared to control conditions.

Our in silico model is based on a recently described characterization of human hippocampal GC recordings[42]. Because one

https://doi.org/10.1038/s41593-024-01782-5

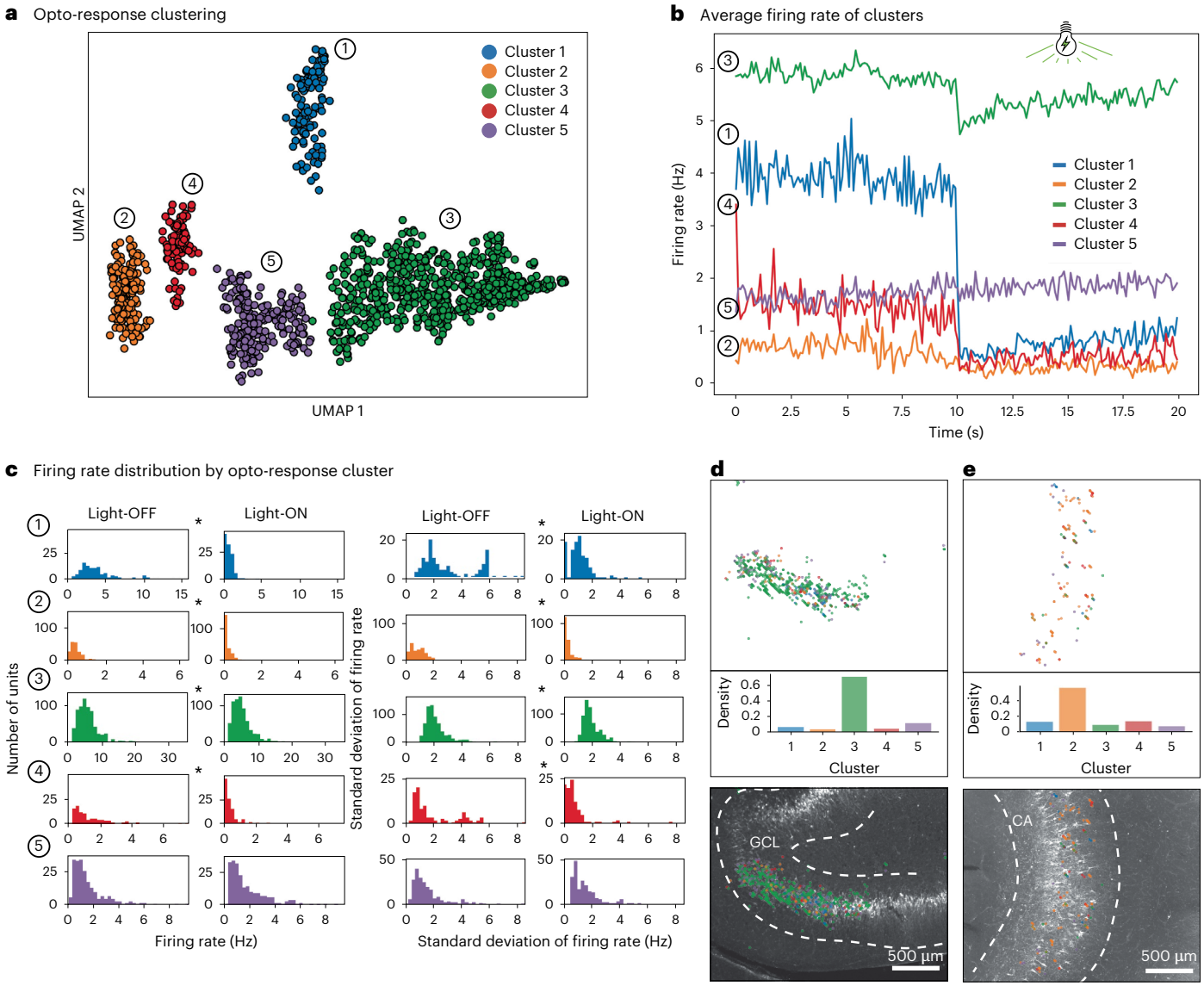

Fig. 6 | Opto-response clustering. a, UMAP of units clustered through an HDBSCAN pipeline of a 20-s period of time correlating with 10 s of time before light-ON and 10 s during light-ON. **b**, Average firing rates for units in each cluster over the course of the analyzed 20-s period. **c**, Firing rate (left) and standard deviation of firing rate (right) of each cluster showing the distributions during light-OFF and light-ON periods. * indicates significant differences in firing rate or firing rate standard deviation between light-ON and light-OFF conditions. Mean and standard deviation distributions were compared with a two-sided Kolmogorov–Smirnov test, considered statistically significant if $P < 0.05$ after correction for multiple comparisons. *P* values for firing rate light-OFF versus light-ON comparisons (left two columns): cluster 1 $P = 2.5 \times 10^{-45}$, cluster 2 $P = 0.0014$, cluster 3 $P = 7.29 \times 10^{-24}$, cluster 4 $P = 1.36 \times 10^{-16}$, cluster 5 $P = 0.0741$. *P* values for firing rate standard deviation light-OFF versus light-ON comparisons (right two columns): cluster 1 $P = 6.43 \times 10^{-25}$, cluster 2 $P = 0.0002$, cluster 3 $P = 1.28 \times 10^{-21}$, cluster 4 $P = 9.38 \times 10^{-13}$, cluster 5 $P = 0.174$. **d**,**e**, Recording areas covering two distinct hippocampal regions known to have disparate cell types. Density histograms beneath each represent the fraction of units in the slice depicted that were assigned to each cluster. The GCL of the dentate gyrus in slice 10F (**d**) and Cornu Ammonis (CA) in slice 3C (**e**). Opto-response cluster identity color is overlaid onto its respective unit locations. Unit locations are shown without (top) and with (bottom) histology underlaid. White immunohistochemistry demonstrates HcKCR1–eYFP expression. Cluster 3 was found to be positively correlated with GCL waveform clusters (z-score 3.28; Supplementary Table 3) using a chi-square test with analysis of standardized residuals (see Methods 'Waveform cluster association with opto-response clusters' subsection). This standardized residual was judged to be significant if greater in magnitude than a critical value of 3.23 calculated for a two-tailed test with the Bonferroni-adjusted significance level. Statistical results of opto-response to waveform cluster correlations are reported in Supplementary Table 6.

limitation of human brain slice experiments is the scarcity of tissue specimens, this model allowed us to predict that even relatively low rates of transduction and inhibition of excitatory neurons could have network-wide effects without extensive tissue use. We envision that experimental design studies involving human tissue could involve an iterative framework involving biophysical models to predict cell type and network effects of perturbations, followed by experimentally testing and refinement. Advances in biophysical modeling of brain networks could, thus, markedly reduce overall needs for human tissue material[42,58–61].

One notable aspect of the observed rhythmic bursting activity was the strong local field potential coherence in the theta frequency band. Waves of coherence in the hippocampus, particularly in theta[62], were described in both human[63–65] and non-human[66–68] hippocampal preparations. HD-MEA recordings of this density have not been reported in the human hippocampus. This high level of resolution allowed for

visualization of waves of theta phase coherence across the GCL of the dentate gyrus (Fig. 4 and Supplementary Videos 3 and 4). This wave of propagation across the GCL is consistent with previous work showing that GCs of the dentate gyrus receive a large amount of excitatory input that is often phase locked with theta frequency local field potential[69]. Given evidence suggesting that epileptiform discharges in the human brain are waves arising from an epileptogenic focus[70], better characterization of such wave propagation may have importance for elucidating epileptic circuits. These data demonstrate the utility of the HD-MEA platform used here to characterize network synchronization patterns as a potential target for therapeutic intervention.

The ability to record dozens to hundreds of neurons simultaneously is one of the advantages of the HD-MEA recording platform described here. Such high-throughput methods may be effective for hypothesis generation about the neuronal ensemble and cell type responses that can be validated with experiments based on patch-clamp or Patch-seq[71]. We used clustering techniques to leverage these advantages of the platform. We probed whether differences in neuronal cell type might contribute to differences in optogenetic response in our data, because many factors can affect neuronal responses, even to the same ligand[72]. The waveform clustering method distinguishes putative neuronal cell types based on extracellular spike waveform features (Fig. 5)[52,53]. To test whether the clustering results were reasonable, we used the anatomic localization of our slice recordings. The GCL is composed mostly of GC neurons, which are not typically found elsewhere in the hippocampus[73–76]. Comparing the distribution of waveform clusters from recordings over the GCL to recordings not over the GCL, five clusters were significantly associated with localization over the GCL (Fig. 5), suggesting that these may represent GCL neurons.

We used an unsupervised clustering (HDBSCAN[54,55,77,78]) approach to distinguish patterns of neuronal response to optogenetic HcKCR1 activation that may not be captured by firing rate averages. Rather than simply clustering into responders and non-responders to slice illumination, this approach yielded five opto-response clusters (Fig. 6). The waveform clusters associated with GCL histologic localization (clusters 5, 6, 8, 9 and 10 from Fig. 5) were overrepresented in opto-response cluster 3 (Supplementary Table 6), which had, on average, a high baseline firing rate and modest reduction during slice illumination (Fig. 6b,c). This suggested that cell type—in this case GC identity—may play a role in optogenetic response to HcKCR1 activation, although activity state at the time of slice illumination cannot be ruled out based on these analyses[40]. Single-nucleus sequencing data suggest that GCs typically express CAMK2A at high levels compared to other hippocampal neurons[79], such that promoter gene expression does not completely explain this modest reduction in firing rate seen during HcKCR1 activation in putative GCL neurons. These clustering techniques explain some of the heterogeneity of network and neuronal response to HcKCR1 activation in a subset of CAMK2A+ neurons, but there are limits on the conclusions that can be drawn from them. Our initial hypothesis was that the HDBSCAN analyses of firing rate response would yield two distinct clusters of responders and non-responders to light-ON conditions that might serve as a surrogate for HcKCR1 expression. The results, however, present a more complicated picture. Cell type, HcKCR1 expression and connectivity between neurons expressing and not expressing HcKCR1 are all likely contributing to the larger picture. Additional analyses of how individual neurons respond and influence one another will be necessary to make conclusions of how manipulating a subset of neurons in a hippocampal slice affects network activity.

In the present work, we used hippocampi resected en bloc from patients with drug-resistant temporal lobe epilepsy. Clinically, these hippocampi were determined to be likely or definitively involved in generating seizure activity. By this definition, the hippocampi recorded may have physiologic differences from what might be considered normal physiology or connectivity in non-epileptic human tissue. Although this caveat should be noted when making biological conclusions about hippocampal function, it should also be noted that the intended target for prospective epilepsy therapies is epileptogenic hippocampi. This makes the preparation presented here an optimal model for pathologic insights but, perhaps, limited in regard to normal hippocampal physiology.

Emerging strategies to develop AAVs with improved fidelity and robustness[30] harness methods for screening synthetic libraries of capsid proteins as well as enhancer elements[29,30,80–82]. AAV gene delivery studies have thus far focused on visualizing transduced neurons and describing their relevance with regard to normal central nervous system (CNS) physiology[32,80,83]. Such investigations would benefit from characterizing how these tools can be used in pathologic circuits. Ex vivo cultures of human brain slices may both accelerate the development of such tools and serve as a platform for investigating the circuit-level effects of AAV-mediated, gain-of-function gene delivery. The techniques described herein allow for a layer of functional screening of AAVs for gene delivery by combining validation of human brain tissue expression with the potential to measure electrophysiologic activity and circuit-level effects.

The field of surgical treatment of epilepsy is evolving at a rapid pace. Although surgical resection is the gold standard for drug-refractory focal epilepsy[84], responsive neurostimulation is another increasingly common treatment for select patients[85]. Responsive neurostimulation involves running electrical current though neural tissue using stereotactically implanted electrodes. Neurostimulation techniques do confer clinical reductions in seizure frequency[86], but the mechanism by which they modulate seizures is a topic of ongoing research[87]. Therapeutic translation of optogenetics for epilepsy is still theoretical[88]. The chronic effects and toxicity profiles of optogenetics in human hippocampal neurons require further study[89]. However, permanent implantation of electrodes and power sources into patients with refractory epilepsy and other functional neurologic diseases is now routinely practiced[90–97]. Because such treatments are well received by patients and clinicians, our working hypothesis is that the invasiveness of implanting a light guide and battery will not be the rate-limiting factor in developing therapeutic optogenetics. The lack of models for testing therapeutics in human tissue, on the other hand, may well impede progress on the many experimental fronts that would be necessary for moving in a translational direction[88].

In conclusion, primary human tissue can serve as an experimental platform for optimizing and testing strategies to modulate network activity with the long-term goal of de-risking potential therapeutic interventions. Emerging technologies could enable rapid and scalable genetic access into cell types that could be tested in such ex vivo preparations. Here we describe a scenario whereby AAV-mediated delivery of inhibitory channelrhodopsin into a subset of CAMK2A+ neurons can be used to demonstrate network-wide activity modulation in human hippocampus. These techniques were previously relegated to animal modeling experiments. This study highlights the potential for human brain tissue to serve as a viable model for illuminating human brain neurophysiology.

Online content

Any methods, additional references, Nature Portfolio reporting summaries, source data, extended data, supplementary information, acknowledgements, peer review information; details of author contributions and competing interests; and statements of data and code availability are available at https://doi.org/10.1038/s41593-024-01782-5.

References

1. Staley, K. Molecular mechanisms of epilepsy. *Nat. Neurosci.* **18**, 367–372 (2015).
2. Staley, K. J. & Dudek, F. E. Interictal spikes and epileptogenesis. *Epilepsy Curr.* **6**, 199–202 (2006).

3. Paz, J. T. & Huguenard, J. R. Microcircuits and their interactions in epilepsy: is the focus out of focus? *Nat. Neurosci.* **18**, 351–359 (2015).
4. Crick, F. H. Thinking about the brain. *Sci. Am.* **241**, 219–233 (1979).
5. Boyden, E. S. Optogenetics and the future of neuroscience. *Nat. Neurosci.* **18**, 1200–1201 (2015).
6. Lin, S.-C., Deisseroth, K. & Henderson, J. M. Optogenetics: background and concepts for neurosurgery. *Neurosurgery* **69**, 1–3 (2011).
7. Boyden, E. S., Zhang, F., Bamberg, E., Nagel, G. & Deisseroth, K. Millisecond-timescale, genetically targeted optical control of neural activity. *Nat. Neurosci.* **8**, 1263–1268 (2005).
8. Gradinaru, V. et al. Molecular and cellular approaches for diversifying and extending optogenetics. *Cell* **141**, 154–165 (2010).
9. Zhang, F. et al. Optogenetic interrogation of neural circuits: technology for probing mammalian brain structures. *Nat. Protoc.* **5**, 439–456 (2010).
10. Krook-Magnuson, E., Armstrong, C., Oijala, M. & Soltesz, I. On-demand optogenetic control of spontaneous seizures in temporal lobe epilepsy. *Nat. Commun.* **4**, 1376 (2013).
11. Krook-Magnuson, E. et al. In vivo evaluation of the dentate gate theory in epilepsy. *J. Physiol.* **593**, 2379–2388 (2015).
12. Fradot, M. et al. Gene therapy in ophthalmology: validation on cultured retinal cells and explants from postmortem human eyes. *Hum. Gene Ther.* **22**, 587–593 (2011).
13. Sahel, J.-A. et al. Partial recovery of visual function in a blind patient after optogenetic therapy. *Nat. Med.* **27**, 1223–1229 (2021).
14. Avoli, M. et al. Epileptiform activity induced by low extracellular magnesium in the human cortex maintained in vitro. *Ann. Neurol.* **30**, 589–596 (1991).
15. Masukawa, L. M., Higashima, M., Kim, J. H. & Spencer, D. D. Epileptiform discharges evoked in hippocampal brain slices from epileptic patients. *Brain Res.* **493**, 168–174 (1989).
16. Cohen, I., Navarro, V., Clemenceau, S., Baulac, M. & Miles, R. On the origin of interictal activity in human temporal lobe epilepsy in vitro. *Science* **298**, 1418–1421 (2002).
17. Köhling, R. & Avoli, M. Methodological approaches to exploring epileptic disorders in the human brain in vitro. *J. Neurosci. Methods* **155**, 1–19 (2006).
18. Andersson, M. et al. Optogenetic control of human neurons in organotypic brain cultures. *Sci. Rep.* **6**, 24818 (2016).
19. Ledri, M., Andersson, M., Wickham, J. & Kokaia, M. Optogenetics for controlling seizure circuits for translational approaches. *Neurobiol. Dis.* **184**, 106234 (2023).
20. Wykes, R. C. et al. Optogenetic and potassium channel gene therapy in a rodent model of focal neocortical epilepsy. *Sci. Transl. Med.* **4**, 161ra152 (2012).
21. Wykes, R. C., Kullmann, D. M., Pavlov, I. & Magloire, V. Optogenetic approaches to treat epilepsy. *J. Neurosci. Methods* **260**, 215–220 (2016).
22. Jones, R. S., da Silva, A. B., Whittaker, R. G., Woodhall, G. L. & Cunningham, M. O. Human brain slices for epilepsy research: pitfalls, solutions and future challenges. *J. Neurosci. Methods* **260**, 221–232 (2016).
23. Grone, B. P. & Baraban, S. C. Animal models in epilepsy research: legacies and new directions. *Nat. Neurosci.* **18**, 339–343 (2015).
24. Bosque, J. R. et al. Molecular tools for the characterization of seizure susceptibility in genetic rodent models of epilepsy. *Epilepsy Behav.* **121**, 106594 (2021).
25. Lévesque, M., Avoli, M. & Bernard, C. Animal models of temporal lobe epilepsy following systemic chemoconvulsant administration. *J. Neurosci. Methods* **260**, 45–52 (2016).
26. Armstrong, C., Krook-Magnuson, E., Oijala, M. & Soltesz, I. Closed-loop optogenetic intervention in mice. *Nat. Protoc.* **8**, 1475–1493 (2013).
27. Matsuzaki, Y. et al. Intravenous administration of the adeno-associated virus-PHP.B capsid fails to upregulate transduction efficiency in the marmoset brain. *Neurosci. Lett.* **665**, 182–188 (2018).
28. Hordeaux, J. et al. The neurotropic properties of AAV-PHP.B are limited to C57BL/6J mice. *Mol. Ther.* **26**, 664–668 (2018).
29. Zhu, D. et al. Optimal trade-off control in machine learning based library design, with application to adeno-associated virus (AAV) for gene therapy. *Sci. Adv.* **10**, eadj3786 (2024).
30. Zhu, D., Schieferecke, A. J., Lopez, P. A. & Schaffer, D. V. Adeno-associated virus vector for central nervous system gene therapy. *Trends Mol. Med.* **27**, 524–537 (2021).
31. Chen, X. et al. Engineered AAVs for non-invasive gene delivery to rodent and non-human primate nervous systems. *Neuron* **110**, 2242–2257 (2022).
32. Goertsen, D. et al. AAV capsid variants with brain-wide transgene expression and decreased liver targeting after intravenous delivery in mouse and marmoset. *Nat. Neurosci.* **25**, 106–115 (2022).
33. Chan, K. Y. et al. Engineered AAVs for efficient noninvasive gene delivery to the central and peripheral nervous systems. *Nat. Neurosci.* **20**, 1172–1179 (2017).
34. Deverman, B. E., Ravina, B. M., Bankiewicz, K. S., Paul, S. M. & Sah, D. W. Gene therapy for neurological disorders: progress and prospects. *Nat. Rev. Drug Discov.* **17**, 641–659 (2018).
35. Andrews, M. R. Gene therapy in the CNS—one size does not fit all. *Gene Ther.* **28**, 393–395 (2021).
36. Ting, J. T. et al. A robust ex vivo experimental platform for molecular-genetic dissection of adult human neocortical cell types and circuits. *Sci. Rep.* **8**, 8407 (2018).
37. Le Duigou, C. et al. Imaging pathological activities of human brain tissue in organotypic culture. *J. Neurosci. Methods* **298**, 33–44 (2018).
38. Schwarz, N. et al. Long-term adult human brain slice cultures as a model system to study human CNS circuitry and disease. *eLife* **8**, e48417 (2019).
39. Blümcke, I. et al. International consensus classification of hippocampal sclerosis in temporal lobe epilepsy: a Task Force report from the ILAE Commission on Diagnostic Methods. *Epilepsia* **54**, 1315–1329 (2013).
40. Govorunova, E. G. et al. Kalium channelrhodopsins are natural light-gated potassium channels that mediate optogenetic inhibition. *Nat. Neurosci.* **25**, 967–974 (2022).
41. Vierock, J. et al. WiChR, a highly potassium-selective channelrhodopsin for low-light one-and two-photon inhibition of excitable cells. *Sci. Adv.* **8**, eadd7729 (2022).
42. Buchin, A. et al. Multi-modal characterization and simulation of human epileptic circuitry. *Cell Rep.* **41**, 111873 (2022).
43. Ma, Z., Turrigiano, G. G., Wessel, R. & Hengen, K. B. Cortical circuit dynamics are homeostatically tuned to criticality in vivo. *Neuron* **104**, 655–664 (2019).
44. Mele, M. et al. Transient incubation of cultured hippocampal neurons in the absence of magnesium induces rhythmic and synchronized epileptiform-like activity. *Sci. Rep.* **11**, 11374 (2021).
45. Mody, I., Lambert, J. & Heinemann, U. Low extracellular magnesium induces epileptiform activity and spreading depression in rat hippocampal slices. *J. Neurophysiol.* **57**, 869–888 (1987).
46. Keller, C. J. et al. Heterogeneous neuronal firing patterns during interictal epileptiform discharges in the human cortex. *Brain* **133**, 1668–1681 (2010).
47. Lévesque, M. & Avoli, M. The kainic acid model of temporal lobe epilepsy. *Neurosci. Biobehav. Rev.* **37**, 2887–2899 (2013).
48. Vezzani, A. et al. Interleukin-1β immunoreactivity and microglia are enhanced in the rat hippocampus by focal kainate application: functional evidence for enhancement of electrographic seizures. *J. Neurosci.* **19**, 5054–5065 (1999).

49. Jimenez-Mateos, E. M. et al. Silencing microRNA-134 produces neuroprotective and prolonged seizure-suppressive effects. *Nat. Med.* **18**, 1087–1094 (2012).
50. Huberfeld, G. et al. Glutamatergic pre-ictal discharges emerge at the transition to seizure in human epilepsy. *Nat. Neurosci.* **14**, 627–634 (2011).
51. Herman, A. M., Huang, L., Murphey, D. K., Garcia, I. & Arenkiel, B. R. Cell type-specific and time-dependent light exposure contribute to silencing in neurons expressing Channelrhodopsin-2. *eLife* **3**, e01481 (2014).
52. Lee, E. K. et al. Non-linear dimensionality reduction on extracellular waveforms reveals cell type diversity in premotor cortex. *eLife* **10**, e67490 (2021).
53. Lee, K., Carr, N., Perliss, A. & Chandrasekaran, C. WaveMAP for identifying putative cell types from in vivo electrophysiology. *STAR Protoc.* **4**, 102320 (2023).
54. Masuda, F. K., Aery Jones, E. A., Sun, Y. & Giocomo, L. M. Ketamine evoked disruption of entorhinal and hippocampal spatial maps. *Nat. Commun.* **14**, 6285 (2023).
55. McInnes, L. & Healy, J. Accelerated hierarchical density based clustering. In *Proc. of the 2017 IEEE International Conference On Data Mining Workshops (ICDMW)* (eds Gottumukkala, R. et al.) https://doi.org/10.1109/ICDMW.2017.12 (IEEE, 2017).
56. Tønnesen, J., Sørensen, A. T., Deisseroth, K., Lundberg, C. & Kokaia, M. Optogenetic control of epileptiform activity. *Proc. Natl Acad. Sci. USA* **106**, 12162–12167 (2009).
57. Castillo, P. E., Malenka, R. C. & Nicoll, R. A. Kainate receptors mediate a slow postsynaptic current in hippocampal CA3 neurons. *Nature* **388**, 182–186 (1997).
58. Savtchenko, L. P. et al. Disentangling astroglial physiology with a realistic cell model in silico. *Nat. Commun.* **9**, 3554 (2018).
59. Ecker, A. et al. Data-driven integration of hippocampal CA1 synaptic physiology in silico. *Hippocampus* **30**, 1129–1145 (2020).
60. Chiang, C. C., Shivacharan, R. S., Wei, X., Gonzalez-Reyes, L. E. & Durand, D. M. Slow periodic activity in the longitudinal hippocampal slice can self-propagate non-synaptically by a mechanism consistent with ephaptic coupling. *J. Physiol.* **597**, 249–269 (2019).
61. Schmalz, J., Quinarez, R. V., Kothare, M. V. & Kumar, G. Controlling neocortical epileptic seizures using forced temporal spike-time stimulation: an in silico computational study. *Front. Comput. Neurosci.* **17**, 1084080 (2023).
62. Buzsáki, G. Theta oscillations in the hippocampus. *Neuron* **33**, 325–340 (2002).
63. Kleen, J. K. et al. Bidirectional propagation of low frequency oscillations over the human hippocampal surface. *Nat. Commun.* **12**, 2764 (2021).
64. Zhang, H. & Jacobs, J. Traveling theta waves in the human hippocampus. *J. Neurosci.* **35**, 12477–12487 (2015).
65. Goyal, A. et al. Functionally distinct high and low theta oscillations in the human hippocampus. *Nat. Commun.* **11**, 2469 (2020).
66. Lubenov, E. V. & Siapas, A. G. Hippocampal theta oscillations are travelling waves. *Nature* **459**, 534 (2009).
67. Goutagny, R., Jackson, J. & Williams, S. Self-generated theta oscillations in the hippocampus. *Nat. Neurosci.* **12**, 1491–1493 (2009).
68. Etter, G., van der Veldt, S., Choi, J. & Williams, S. Optogenetic frequency scrambling of hippocampal theta oscillations dissociates working memory retrieval from hippocampal spatiotemporal codes. *Nat. Commun.* **14**, 410 (2023).
69. Pernía-Andrade, A. J. & Jonas, P. Theta-gamma-modulated synaptic currents in hippocampal granule cells in vivo define a mechanism for network oscillations. *Neuron* **81**, 140–152 (2014).
70. Diamond, J. M. et al. Interictal discharges in the human brain are travelling waves arising from an epileptogenic source. *Brain* **146**, 1903–1915 (2023).
71. Cadwell, C. R. et al. Electrophysiological, transcriptomic and morphologic profiling of single neurons using Patch-seq. *Nat. Biotechnol.* **34**, 199–203 (2016).
72. Rahmati, N. et al. Unique actions of GABA arising from cytoplasmic chloride microdomains. *J. Neurosci.* **41**, 4957–4975 (2021).
73. Yao, Z. et al. A taxonomy of transcriptomic cell types across the isocortex and hippocampal formation. *Cell* **184**, 3222–3241 (2021).
74. Mott, D. D., Turner, D. A., Okazaki, M. M. & Lewis, D. V. Interneurons of the dentate–hilus border of the rat dentate gyrus: morphological and electrophysiological heterogeneity.*J. Neurosci.* **17**, 3990–4005 (1997).
75. Jaffe, A. E. et al. Profiling gene expression in the human dentate gyrus granule cell layer reveals insights into schizophrenia and its genetic risk. *Nat. Neurosci.* **23**, 510–519 (2020).
76. Murphy, B. L. et al. Heterogeneous integration of adult-generated granule cells into the epileptic brain. *J. Neurosci.* **31**, 105–117 (2011).
77. Grossberger, L., Battaglia, F. P. & Vinck, M. Unsupervised clustering of temporal patterns in high-dimensional neuronal ensembles using a novel dissimilarity measure. *PLoS Comput. Biol.* **14**, e1006283 (2018).
78. Caldwell, D. et al. Signal recovery from stimulation artifacts in intracranial recordings with dictionary learning. *J. Neural Eng.* **17**, 026023 (2020).
79. Ayhan, F. et al. Resolving cellular and molecular diversity along the hippocampal anterior-to-posterior axis in humans. *Neuron* **109**, 2091–2105 (2021).
80. Mich, J. K. et al. Functional enhancer elements drive subclass-selective expression from mouse to primate neocortex. *Cell Rep.* **34**, 108754 (2021).
81. Deverman, B. E. et al. Cre-dependent selection yields AAV variants for widespread gene transfer to the adult brain. *Nat. Biotechnol.* **34**, 204–209 (2016).
82. Dimidschstein, J. et al. A viral strategy for targeting and manipulating interneurons across vertebrate species. *Nat. Neurosci.* **19**, 1743–1749 (2016).
83. Chuapoco, M. R. et al. Adeno-associated viral vectors for functional intravenous gene transfer throughout the non-human primate brain. *Nat. Nanotechnol.* **18**, 1241–1251 (2023).
84. Wiebe, S., Blume, W. T., Girvin, J. P. & Eliasziw, M. A randomized, controlled trial of surgery for temporal-lobe epilepsy. *N. Engl. J. Med.* **345**, 311–318 (2001).
85. Ma, B. B. & Rao, V. R. Responsive neurostimulation: candidates and considerations. *Epilepsy Behav.* **88**, 388–395 (2018).
86. Razavi, B. et al. Real-world experience with direct brain-responsive neurostimulation for focal onset seizures. *Epilepsia* **61**, 1749–1757 (2020).
87. Khambhati, A. N., Shafi, A., Rao, V. R. & Chang, E. F. Long-term brain network reorganization predicts responsive neurostimulation outcomes for focal epilepsy. *Sci. Transl. Med.* **13**, eabf6588 (2021).
88. Bansal, A., Shikha, S. & Zhang, Y. Towards translational optogenetics. *Nat. Biomed. Eng.* **7**, 349–369 (2023).
89. Priya, R. et al. Activity regulates cell death within cortical interneurons through a calcineurin-dependent mechanism. *Cell Rep.* **22**, 1695–1709 (2018).
90. Nair, D. R. et al. Nine-year prospective efficacy and safety of brain-responsive neurostimulation for focal epilepsy. *Neurology* **95**, e1244–e1256 (2020).

91. Ellens, N. R., Elisevich, K., Burdette, D. E. & Patra, S. E. A comparison of vagal nerve stimulation and responsive neurostimulation for the treatment of medically refractory complex partial epilepsy. *Stereotact. Funct. Neurosurg.* **96**, 259–263 (2018).
92. Haneef, Z. & Skrehot, H. C. Neurostimulation in generalized epilepsy: a systematic review and meta-analysis. *Epilepsia* **64**, 811–820 (2023).
93. Skrehot, H. C., Englot, D. J. & Haneef, Z. Neuro-stimulation in focal epilepsy: a systematic review and meta-analysis. *Epilepsy Behav.* **142**, 109182 (2023).
94. Ma, B. B. et al. Responsive neurostimulation for regional neocortical epilepsy. *Epilepsia* **61**, 96–106 (2020).
95. Panov, F. et al. Safety of responsive neurostimulation in pediatric patients with medically refractory epilepsy. *J. Neurosurg. Pediatr.* **26**, 525–532 (2020).
96. Ryvlin, P. & Jehi, L. E. Neuromodulation for refractory epilepsy. *Epilepsy Curr.* **22**, 11–17 (2022).
97. Ryvlin, P., Rheims, S., Hirsch, L. J., Sokolov, A. & Jehi, L. Neuromodulation in epilepsy: state-of-the-art approved therapies. *Lancet Neurol.* **20**, 1038–1047 (2021).

[1]Department of Neurological Surgery, University of California, San Francisco, San Francisco, CA, USA. [2]Department of Electrical and Computer Engineering, University of California, Santa Cruz, Santa Cruz, CA, USA. [3]UC Santa Cruz Genomics Institute, University of California, Santa Cruz, Santa Cruz, CA, USA. [4]Department of Biomolecular Engineering, University of California, Santa Cruz, Santa Cruz, CA, USA. [5]California Institute for Quantitative Biosciences, University of California, Berkeley, Berkeley, CA, USA. [6]Department of Molecular, Cell & Developmental Biology, University of California, Santa Cruz, Santa Cruz, USA. [7]Department of Bioengineering, University of California, Berkeley, California, CA, USA. [8]Department of Psychiatry and Behavioral Sciences, University of California, San Francisco, San Francisco, CA, USA. [9]Department of Pathology, University of California, San Francisco, San Francisco, CA, USA. [10]Department of Computational Media, University of California, Santa Cruz, Santa Cruz, CA, USA. [11]Weill Institute for Neurosciences, University of California, San Francisco, San Francisco, CA, USA. [12]Department of Chemical and Biomolecular Engineering, University of California, Berkeley, Berkeley, CA, USA. [13]Department of Molecular and Cell Biology, University of California, Berkeley, Berkeley, CA, USA. [14]Helen Wills Neuroscience Institute, University of California, Berkeley, Berkeley, CA, USA. [15]Innovative Genomics Institute (IGI), University of California, Berkeley, Berkeley, CA, USA. [16]Eli and Edythe Broad Center of Regeneration Medicine and Stem Cell Research, University of California, San Francisco, San Francisco, CA, USA. [17]Department of Anatomy, University of California, San Francisco, San Francisco, CA, USA. [18]These authors contributed equally: John P. Andrews, Jinghui Geng, Kateryna Voitiuk. ✉e-mail: edward.chang@ucsf.edu; mteodore@ucsc.edu; tomasz.nowakowski@ucsf.edu

Methods

This research complies with all relevant ethical regulations and was approved by the University of California, San Francisco (UCSF) institutional review board (IRB). Informed consent was obtained from patients before surgical resections for refractory epilepsy. There was no participant compensation. The sex, number and age of participants are detailed in Table 1.

Tissue preparation and culture for HD-MEA recordings

Human hippocampal specimens were obtained from patients undergoing temporal lobectomy with hippocampectomy for refractory epilepsy with UCSF IRB approval. Tissue was transported in artificial cerebrospinal fluid (aCSF) bubbled with carbogen and then sliced into 300-µm sections and recovered sequentially in HEPES-buffered aCSF and culture media. The slices were plated on cell culture inserts to allow for long-term culture at the air–liquid interface. Viral transduction was performed on the day of plating with glass micropipettes. Slices were subsequently plated on HD-MEAs with minimal culture media. For optogenetic recordings, a custom, open-source hardware platform was used with off-the-shelf optoelectronic equipment and 3D-printed components.

Human tissue samples were collected from select neurosurgical cases at UCSF with signed patient consent and approval from the UCSF IRB.

Tissue transport and preparation were adapted from Ting et al.[36]. In brief, tissue was collected in the operating room and put in sterile aCSF of the composition (in mM): 92 NMDG, 2.5 KCl, 1.25 NaH_2PO_4, 30 $NaHCO_3$, 20 HEPES, 25 glucose, 2 thiourea, 5 Na-ascorbate, 3 Na-pyruvate, 0.5 $CaCl_2{\cdot}4\ H_2O$ and 10 $MgSO_4{\cdot}7\ H_2O$. Before collection, the pH of the aCSF was titrated to 7.3–7.4 with hydrochloric acid, and the osmolality was 300–305 mOsm kg^{-1}. The solution was pre-chilled to 2–4 °C and thoroughly bubbled with carbogen (95% O_2/5% CO_2) gas before collection.

Tissue was cut into 300-µm slices submerged in carbogen-bubbled aCSF using a vibratome. Slices were briefly recovered in aCSF warmed to 33 °C before plating on cell culture inserts at the air–liquid interface and incubating at 37 °C in 5% CO_2 incubators.

Tissue was cultured and recorded in a media formulation adapted from previous studies[16,36], referred to in the paper as physiologic media: 15% BME, 15% DMEM/F12 + GlutaMAX, 0.65% PBS, 3% H_2O, 0.91 mM $CaCl_2$, 1.96 mM KCl, 0.81 mM $MgSO_4$, 81.90 mM NaCl, 0.84 mM NaH_2PO_4, 14.0 mM $NaHCO_3$, 0.5 µM $ZnSO_4$, 0.01 µM $CuSO_4$, 0.63 mM D-glucose, 0.14 mM sodium pyruvate, 0.58 mM ascorbic acid, 1.0 mM oxalo-acetic acid, 4.0 mM sodium lactate, 0.57 mM citric acid, 4 mM sodium lactate, 0.27% BSA, 0.001 µM 17β-estradiol, 2.28 µM α-tocopherol, 2.10 µM α-tocopherol-acetate, 0.06 µM corticosterone, 5 mM creatine, 1 mM sodium β-hydroxybutyrate, 5 mM mannitol, 0.2 mM phosphate creatine, 0.5% N-2 supplement, 1,250 U ml^{-1} heparin, 0.01 mM ATP, 0.41 µM insulin, 0.0003 µM tri-iodo-L-thyronine sodium, 0.08 µM superoxide dismutase, 0.05 mM glycerol (10×), 0.5 mM GlutaMAX, 1 µM $MnCl_2$, 1 µM γ-amino-butyric acid, 3 µM glutathione and 8 µM taurine.

Plating slices on HD-MEA

To plate tissue plated on MaxWell high-density MEAs, MEAs were incubated with Matrigel for 1 h and subsequently filled with culture/recording media described above. Slices were floated into the MEA wells, and the media were then aspirated slowly such that the slice descended onto the recording surface. The slice was kept in minimal media for the 2 h, during which recordings were carried out. For $GABA_AR$ blockade, bicuculline dissolved in recording media to a concentration of 2 µM was dripped directly on the tissue slice. For low-Mg media, the physiologic media were made without any Mg ($MgSO_4$) added. For KA experiments, 100 nM KA was dripped directly onto the slice.

Examples are shown of large areas of dense activity recorded in Figs. 1 and 3 and overlaid on Figs. 5g,j and 6d,e. Slices that did not show electrophysiologic evidence of unit activity after plating were excluded from electrophysiologic analyses.

Immunohistochemistry

Immunohistochemistry for NeuN and eYFP in the manuscript was performed with the following antibodies:

NeuN immunohistrochemistry: guinea pig anti-NeuN, Millipore, ABN90, dilution 1:1,000, lot no. 407753. ABN90 is a guinea pig polyclonal version of the anti-NeuN, clone A60 (MAB377), a mouse monoclonal antibody that specifically recognizes the DNA-binding, neuron-specific protein NeuN, which is present in most CNS and peripheral nervous system neuronal cell types of all vertebrates tested. This antibody recognized the N-terminus of Neun. Species cross-reactivity demonstrated to react with mouse and rat. Quality control testing was performed by the supplier (Millipore). eYFP immunohistochemistry: chicken anti-GFP antibody, Aves, GFP-1020, dilution 1:1,000, lot no. GFP3717982. We use the cross-reactivity of this antibody with the related enhanced yellow fluorescent (eYFP) protein for immunohistochemistry.

Green fluorescent protein (GFP) is a naturally fluorescent protein originally derived from jellyfish. GFP has been engineered to produce a vast number of variously colored mutants and fusion proteins which are ubiquitous tools in transgenic science. Antibody clonality: polyclonal. Isotype: IgY. Antibody registry ID: AB_2307313. Quality control was performed by the supplier (Aves Labs).

AAVs

AAV9-CAMK2A-HcKCR1-eYFP: titer 5.00×10^{13} GC ml^{-1}

Company: PackGene, lot no. 12109T

Purity was analyzed according to PackGene company protocols by sodium dodecyl sulfate–polyacrylamide gel electrophoresis (SDS-PAGE), finding no other significant bands.

Endotoxin assay was analyzed by quantitative limulus amebocyte lysate (LAL) assay with <10 EU ml^{-1}.

AAV9-CAMK2A-ChR2-eYFP: titer 2.40×10^{13} GC ml^{-1}

Company: Addgene, lot no. v113177

Purified by iodixanol gradient ultracentrifugation. Purity of AAV preparation was assayed according to Addgene protocols by comparing the relative stoichiometric ratios of the viral capsid proteins VP1, VP2 and VP3. Samples of viral preparations were subjected to PAGE followed by silver staining or SYPRO Red staining, and the molecular weight and relative intensity of the viral capsid proteins were analyzed.

Endotoxin assay was analyzed by quantitative LAL assay with <5 EU ml^{-1}.

Design of optogenetic system

The purpose of the designed hardware platform is to trigger an optogenetic stimulation pulse and observe the response of neurons on a high-density electrode array. The optogenetic system was designed to be easy to replicate and does not require custom printed circuit boards (PCBs) or soldering. Assembly instructions are provided in Supplementary Fig. 1. The bill of materials with pricing is available in Supplementary Table 1. Lid and insert from Fig. 2 are described in detail in the 'Optogenetic 3D-printed insert and lid' subsection in the Methods. Software will be provided in a GitHub repository upon release of the paper.

To run an experiment, the user must specify a calibration CSV file, which contains data on an LED's power output (see 'Optogenetic power density measurement and calculation' subsection). The user also connects to the Arduino over a USB serial port. Afterwards, the program creates a stimulation log CSV file into which the stimulation events with their parameters are recorded. Now, the user can construct their own stimulation sequences and use several helper functions with configurable stimulation pattern templates (Fig. 2f).

As the user runs the experiment, stimulation events are logged in both the stimulation log CSV file and the MaxWell voltage

recording .hdf5 file. The MaxWell .hdf5 file has a field that stores a single bit value representing the GPIO pin signal ('1' for on, '0' for off) for every frame of the recording (every 0.05 ms assuming 20-kHz sampling). Therefore, we can extract at which recording frame the light turned on and at which recording frame the light went back to being off. The CSV log file stores a timestamp of each event as well as the intensity of light used and the duration of ON and OFF requested by the user.

Optogenetic system software low-level functionality

The computer sends the Arduino an integer value over USB serial connection corresponding to the desired intensity. Although the intensity is represented to the user as a decimal number between 0 and 1, it is converted to the nearest proportional integer in the range of the 12-bit digital-to-analog converter (DAC) (0–4,095). The range 0–4,095 was chosen instead of the full 12-bit integer range of 0–4,096 because it more closely corresponded to 0–5-V DAC output when measured on an oscilloscope.

The computer also sends the electrophysiology recording system a signal to set GPIO high. GPIO high is +2.0–3.3 V, and anything less than or close to zero is considered GPIO low. When the GPIO signal is high, the Arduino sends a value to the DAC. Thus, to turn the light on, the computer needs to send a non-zero intensity value to the Arduino and also trigger the recording system to set GPIO high.

Optogenetic 3D-printed insert and lid

The optogenetic insert and lid (Fig. 3b,e) were designed to hold the optical fiber in place inside the MEA recording well while keeping an enclosed environment around the tissue culture.

The insert has a tight transition fit with the round MEA well. The lid slots into the insert and is easy to remove but does not rotate because there are alignment groves between the insert and lid. This combination allows having a sturdy interface with the MEA well while being able to gently remove the lid (that is, to add a drug during the experiment) and keep the fiber in the same relative position after re-inserting.

The lid is designed for a fiber-optic component with a 2.5-mm-diameter fiber-optic cannula, a Ø200-µm core fiber with 0.22 NA and a fiber length of 20 mm (Thorlabs, CFM22L20). The optical fiber was estimated to be 0.95-mm above the MEA sensor based on MEA well measurements and computer-aided design (CAD) model of the assembled components.

The optogenetic insert and lid were 3D printed (on Formlabs Form 3B+) with BioMed Clear V1 material (Formlabs, RS-F2-BMCL-01). Before use in tissue culture, the 3D-printed parts, along with the optical fiber (Thorlabs, CFM22L20) and ceramic mating sleeve (Thorlabs, ADAF1-5), were individually sealed in autoclavable bags (PlastCare, RIT-3565) and steam sterilized either at 134 °C for 20 min or at 121 °C for 30 min.

Activity detection algorithm and closed-loop optical intervention

We implemented an algorithm that monitors spike activity in real time, using data from the HD-MEA (Fig. 3). This algorithm is meant to demonstrate a therapeutic use-case scenario. When a predefined spike threshold is detected, the algorithm triggers illumination of the slice. Spike activity was measured by counting the total number of 5-root-mean-square (rms) spikes that occurred in 10 s across all the electrodes on the HD-MEA.

Experimentally, this threshold was to be 2–4 times above the average baseline 5-rms spike activity for 1 min before application of bicuculline. After the drug was applied, activity quickly surpassed this threshold. After the threshold is surpassed for a 10-s window, the algorithm triggers 10 s of illumination. Afterwards, the algorithm goes back to monitoring activity. This algorithm is intentionally simple in nature, to provide a proof of concept that user-defined signals can be detected in real time using HD-MEA interface with this ex vivo model, in a closed-loop process.

Optogenetic power density measurement and calculation

Power output for the optical fiber was measured with Thorlabs meter PM100D with sensor S130C. The power density (mW mm^{-2}) values of the light presented here were calculated by dividing the measured power by the cross-sectional area of the fiber, using this formula:

For multimode fiber with Ø200-µm core:

$$\text{Beam radius} = r = \left(\frac{200\mu m}{2}\right) = 100\mu m = 0.100mm$$

$$\text{Average power} = P_{avg}$$

$$\text{Surface power density} = \frac{P_{avg}}{\pi r^2} = \text{mW/mm}^2$$

where P_{avg} is measured power, and r is ½ the fiber core diameter. For additional information of how these data were collected, see the extended data optogenetic power density measurement and calculation.

A Python script was used to automatically control the light intensity with the Arduino and take samples with the Thorlabs PM100D and then plot the calibration curves for output power. The calibration data along with parameters of the hardware (the fiber core diameter, LED wavelength and LED driver maximum current limit) are saved in a separate calibration CSV file. The user must import the calibration data CSV file to start an experiment. Power density (mW mm^{-2}) was calculated each time by the Python script using the formula. The user can measure different LEDs and use the calibration files to convert between intensity (0–1 value) and mW mm^{-2} values during experiments and analysis.

Data acquisition

Neuronal activity was sampled simultaneously at 20 kHz from multiple electrodes on the HD-MEA for both action potential and local field potential bandwidth. During the experiment, an activity scan assay using MaxLab Interface across all 26,400 electrodes was performed first, and then a maximum of 1,024 available channels were manually selected to record from the most active areas spread across the MEA. Closed-loop seizure detection and optical intervention started after the assay from a custom Python script. After the experiment, raw activity data and optical stimulation timestamps were saved to an .hdf5 file on local memory. The optical light protocol was written into a separate CSV logging file pairing with the raw data (see the 'Design of optogenetic system' subsection).

Spike sorting

Kilosort2 (ref. 98) was used for sorting the raw data into single-unit activity. Because the high-density MEA can record one neuron from tens of channels, it is common that the spikes from many neurons overlap in time for a single channel. The template matching and clustering algorithm in Kilosort2 can distinguish spikes between different neurons based on their waveform and assign them to individual clusters. Raw data were bandpass filtered with 300–6,000 Hz and sorted in Kilosort2 with a voltage detection threshold of 6 rms over the baseline. Spike sorting was performed on the Pacific Research Platform computing cluster with an NVIDIA GeForce GTX 1080 Ti GPU. For spike sorting, both manual and auto-curation techniques were applied (see below). Kilosort2's result was manually curated using Phy GUI[99] by experienced electrophysiology researchers. The quality metrics[100] for saving high-quality units are based on the shape of the spike waveform, firing rate and inter-spike interval (ISI) distribution.

We applied both auto-curation and manual curation to evaluate the integrity and physiologic relevance of each single-unit output from spike sorting. We developed an auto-curation technique to allow for expedient curation of large numbers of units sometimes recorded on the HD-MEA. Comparing the results of auto-curation versus manual curation, we found that auto-curation was, in general, more

conservative (that is, excluded more units). For auto-curation results that led to disparities from manually curated recordings (including slices 5C, 7D and 8D), we deferred to manual curation results to avoid undersampling the network activity.

The manual curation process involved evaluating spike waveforms based on morphological characteristics and spatial distribution, calculating unit minimum firing rates and assessing ISI violation ratios. We checked the morphology of the spike waveform and spatial distribution on the electrodes, preserving the high-quality waveforms that follow the biophysical properties of an action potential generation, showcasing a reasonable duration, amplitude and a clear peak and trough and exhibiting coherent waveform patterns across neighboring channels relative to the unit's identified location on the MEA.

The firing rate for each unit was calculated using the equation

$$rate = N_{spikes}/T_{rec}$$

where N_{spikes} represents the total number of spikes, and T_{rec} denotes the duration of the recording in seconds. Units that had less than 0.1-Hz firing rate were excluded from further analysis.

Additionally, the ISI violation ratio was assessed for each unit because it serves as an indicator of refractory period violation. The ISI violation ratio is defined as the total number of ISIs that are shorter than 1.5 ms relative to the total number of spikes. Units exhibiting more than a 10% ISI violation ratio were considered to have significant refractory period contamination and were, thus, removed from the dataset.

The auto-curation process was applied to the output of spike sorting by executing a Python script, as detailed in the associated GitHub repository: https://github.com/braingeneers/AndrewsGengVoitiukEtAl_SourceCode.

Within this script, we used curation functions from the SpikeInterface API curation module to evaluate quality metrics, such as the signal-to-noise ratio (SNR), ISI violation ratio, firing rate and waveform spatial distribution for each unit. The SNR was determined using the compute_snrs function with a threshold set at 5 rms. Calculation of the ISI violation ratio employed the Hill method[101], facilitated by the compute_isi_violations function, with 1.5 ms as the threshold for identifying refractory period violations and a 20% violation rate for excluding a unit from further analysis. The firing rate threshold was 0.1 Hz. Waveforms were extracted for each unit across all active channels using the WaveformExtractor class, averaging up to 500 spikes. These waveforms were then sorted by amplitude. Units lacking coherent waveform patterns across the eight nearest neighbor channels within a 17.5-µm diameter were excluded.

Propagation of epileptiform activity by firing rate

The propagation of epileptiform activity (Fig. 4c) was observed through an increase in firing rate during rhythmic bursting. For each individual unit, the baseline firing rate was determined by the number of regular spiking activities within the first 5 s of the recording. The increase in firing rate was assessed by comparing the spike activity during the burst against the baseline. To identify the burst period, the population firing rate of all units was measured in 100-ms continuous bins and smoothed with a Gaussian kernel (sigma = 5). The peak firing rate timepoint (t_p) was determined using the SciPy function find_peaks, with a 2-s window centered around t_p. Given the sequential nature of the units' firing activity within the burst, this time window was further divided into 20 sub-windows of 100 ms each. A threshold set at 3 s.d. above the baseline firing rate was applied to each unit within these sub-windows. The locations on the MEA of units surpassing this threshold were plotted, and the corresponding spike events were marked in red on the raster plot.

Activity heatmaps

Activity heatmaps in Figs. 1 and 3 show the spatial distribution of significant voltage events. The MaxWell software computes a moving rms value for each electrode, and we used this to determine events that crossed a threshold set at 5× the rms value of each respective electrode. A 2D spatial grid of the counts per second was constructed, and then a 2D Gaussian blur with radius, r, was used to enable better visual continuity. Each position in the grid was divided by $2\pi r^2$ so the values displayed would correspond to events per second, making it so the Gaussian blur does not significantly alter the values of each data point. These values were then plotted as the activity heatmaps, where warmer colors represent areas of higher event frequency, and darker colors denote regions with less activity.

Statistics and reproducibility

Sample sizes were maximized based on the availability of human brain tissue samples. There was no randomization. Samples were processed and experiments run in the order that patient tissue became available. No statistical method was used to predetermine sample size, but our sample sizes are similar to those reported in previous publications[10,20,50]. The experiments were not randomized. Data collection and analysis were not performed blinded to the conditions of the experiments. Much of the statistical analyses involved comparing neuronal activity during a time period during which light was shone on the slice and comparing that data to periods of time immediately preceding and following this 'light-ON' time period. As such, knowing these exact timepoints was necessary for accurate analysis. Data distribution was assumed to be normal, but this was not formally tested.

Inclusion and exclusion criteria

All slices included in electrophysiologic analyses were from adult patients with refractory epilepsy and were cultured for 4–8 d before recordings. Acute recordings were excluded from waveform clustering analyses. Any slice from which unit activity was not recorded after plating on HD-MEAs was not included in electrophysiologic analyses.

For transparency, no slices showing HD-MEA data that were transduced with HcKCR1 were excluded from analyses. These slices are shown in Extended Data Figs. 4–6. Waveform clustering analyses used data from all slices in Table 1. Opto-response clustering analyses included all slices that were transduced with HcKCR1 and yielded unit activity, listed in Table 2 and shown in Extended Data Figs. 4–6.

Firing rate and amplitude

To compare firing rate and amplitude (Extended Data Figs. 4–6 and 8) across multiple trials for the groups 'pre', 'light-ON' and 'light-OFF', we calculated the mean firing rate (and spike amplitude) of each recorded neuronal unit across trials in each slice for their respective experimental conditions. We then used a two-tailed, paired t-test with the t.test() function in R. To correct for multiple comparisons, we used Holm–Bonferroni correction for multiple comparisons using P.adjust with method = 'holm'. The n for each individual trial comparison was calculated from the number of units recorded per trial and is listed in the figure legends. This was done in RStudio 2022.07.1, Build 554.

Mean relative firing rate reduction

In Supplementary Fig. 3, we compare differences in magnitude of firing rate reduction from optogenetic activation between conditions exogenously increasing glutamatergic tone (low Mg with and without KA) versus those without exogenous glutamatergic tone (physiologic media with and without bicuculline). To do this, we calculated mean firing rates of all units during the 10 s before light-ON and the 10 s during light-ON. Slices were grouped in the following fashion: for the physiologic media with and without bicuculline (Physio + Bic), one slice with physiologic media only and three slices after addition of bicuculline ($n = 4$). For 0-Mg, $n = 4$ slices were recorded with low-Mg media. For 0-Mg + KA, the same $n = 4$ slices were recorded for the 0-Mg condition, using the recordings after administration of KA. For each slice, the mean firing rate was calculated for the 10 s before light-ON

and the 10 s during light-ON, and the difference between the firing rates for each slice was expressed as a percent change from 10 s before light-ON to 10 s during light-ON (for example, if the mean firing rate before light-ON was 10 Hz and the mean firing rate during light-ON was 7.5 Hz, this would be as 25% change in firing rate). Two-tailed Welch's *t*-tests were used for individual comparisons.

Waveform clustering for cell typing

The correlation between cell type and extracellular waveforms was explored to discern putative cell types across different brain regions within hippocampal slices (Fig. 5). Waveform clustering was performed using the WaveMAP Python package[53] that combines nonlinear dimensionality reduction with graph clustering. Key algorithms employed include uniform manifold approximation and projection (UMAP) and Louvain clustering methodologies.

To extract the spike waveform for each individual unit, raw recordings were spike sorted using Kilosort2, followed by auto-curation to get high-quality single-unit activity. Waveforms were then averaged across up to 500 spikes within a 5-ms window, using data from the channel capturing the neuron's largest amplitude. Before input into the clustering algorithm, all waveforms were centered at their peak, truncated to 1 ms before and 1.5 ms after the peak. Positive spikes were excluded considering their high possibility of axonal potentials[102]. Subsequently, the waveforms were saved to a NumPy array and processed by l2 normalization. The total number of waveforms was 3,681, gathered from 66 recordings on 12 slices.

UMAP parameters were configured with 20 neighbors and a minimum distance of 0.1, whereas Louvain clustering resolution was set to 1.5, resulting in the identification of 12 distinct clusters by the algorithm.

Waveform cluster association with GCL

To assess the association between waveform clusters (Fig. 5) and their anatomical localization within the GCL, we used R software (version 2022.07.1, Build 554). Given the binary nature of our dependent variable (presence versus absence of a unit within the GCL), we used logistic regression analysis. This choice was predicated on the need to understand the extent to which belonging to a specific cluster could predict the likelihood of a neuronal unit being located in the GCL, with clusters serving as categorical predictor variables in the model.

Before analysis, neuronal unit data were rigorously cleaned and formatted. Each unit was classified into one of 12 clusters based on waveform features, with this classification serving as independent variables in our subsequent logistic regression model. The dependent variable was binary, denoting the anatomical attribution of each unit to either the GCL (1) or other hippocampal regions (0). Logistic regression was then performed using the 'glm' function in R, specifying a binomial family to accommodate our binary dependent variable. The model included one intercept and individual coefficients for each cluster, allowing us to estimate the odds ratio of GCL localization for units in each cluster relative to the baseline condition (absence from GCL).

To address potential type I errors due to multiple comparisons—given the 12 clusters analyzed—we implemented a *P* value adjustment using the Benjamini–Hochberg method. Adjusted confidence intervals and *P* values were calculated and are reported in Supplementary Table 2.

Waveform cluster association with opto-response clusters

To examine the association between neuronal unit classifications based on waveform cluster identity (Fig. 5) and opto-response cluster identity (Fig. 6), we employed a two-step statistical approach. Initially, a chi-square test of independence was applied to a contingency table representing the distribution of units across the predetermined cluster identities (RStudio function: chisq.test). This test assesses the null hypothesis that waveform and opto-response cluster identities are independent of each other across the entire dataset. Given the categorical nature of our data, where each unit is classified into discrete clusters based on spike waveform morphology and optogenetic response, the chi-square test provides a suitable framework for detecting overall patterns of association between these two classification methods. However, the chi-square test alone does not indicate which specific cluster associations contribute to the overall significance. Thus, we conducted a post hoc analysis using standardized residuals, which, in this context, functions analogously to z-scores. For each cell in the contingency table, the standardized residual calculates the number of standard deviations that the observed frequency is from the expected frequency, under the assumption of independence. These residuals thus provide a measure of the magnitude and direction of deviation for each cluster association, enabling us to identify specific pairs of waveforms and opto-response clusters that are associated more or less frequently than would be expected by chance alone. Standardized residuals are computed as follows:

$$\text{Standardized Residual} = \left(\frac{O - E}{\sqrt{E}}\right)$$

where O represents the observed frequency in each cell, and E denotes the expected frequency, calculated based on the marginal totals under the assumption of independence. We applied a Bonferroni correction to control for the family-wise error rate. This correction adjusts the significance threshold by dividing the conventional alpha level (0.05) by the number of comparisons made. A comparison is considered statistically significant if its absolute standardized residual exceeds the critical value derived from the Bonferroni-adjusted alpha of 0.05.

Peristimulus histogram clustering

For the clustering displayed in Fig. 6, the response of individual units to optogenetic stimulus was reduced to a peristimulus histogram and then clustered using a combination of the UMAP[103] and HDBSCAN[55] algorithms to yield the five clusters discussed in the main text.

Peristimulus histograms were computed as the mean spike counts in each of the 1-ms timebins in the 10-s period before plus the 10-s period after the optogenetic stimulus. This is also an estimate of the mean firing rate of the unit as a function of stimulus-relative time, with units of 1 / bin size, here equivalent to kHz.

As a pre-processing step for clustering, the peristimulus histograms were normalized to have the same maximum value. UMAP was then applied to reduce the dimensionality from 200 to 10, with the number of neighbors set to 10 and the minimum distance set to zero. Varying these parameters affects the quality of the clustering but does not change the conclusions except by reducing cluster quality. Clustering was performed on the UMAP output by HDBSCAN with $\varepsilon = 0.35$ and a minimum cluster size of 50. Results were visualized using principal component analysis (PCA) to reduce the 10-dimensional UMAP to two dimensions, but no analysis was performed on the output of PCA.

To compute whether a given cluster had a significant response to optogenetics, for each unit the mean and standard deviation of the instantaneous firing rate were computed separately over the pre-stimulus and post-stimulus periods. This yields two pairs of distributions, which were compared using the two-sided Kolmogorov–Smirnov test. If both the mean and standard deviation were different between the two time periods at a $P < 0.05$ significance level after multiple hypothesis correction, we considered the cluster opto-responsive.

Kullback–Liebler divergence and phase coherence

To represent phase coherence events in time of the local field potentials (Fig. 3g–i), we first constructed an analytic (complex-valued) time series using the Hilbert transform extension. We then extracted the instantaneous phase distributions at each instant and measured the divergence between these and a uniform null hypothesis using the

Kullback–Liebler divergence (KLD). Let χ be a binning of the interval [0, 2π]. Furthermore, let $P_\chi(t)$ be the probability distribution of the phase angle values at time t, and let Q_χ be the uniform distribution with respect to χ. Our entropy-based metric of coherence across time is defined as

$$K(t) = D(P_\chi(t)||Q_\chi) = \sum_{x\in\chi} P_\chi(x)\log\left(\frac{P_\chi(x;t)}{Q_\chi(x)}\right)$$

By inspection of the polar histograms, it was determined that, in many cases, the nature of the distribution deviated considerably from a Von Mises distribution, making the *P* value a misleading measure of coherence. In the field of mathematical statistics, the KLD serves as a statistical distance, quantifying the discrepancy between a given probability distribution *P* and a reference probability distribution *Q*, making it a better indicator of phase coherence when the reference *Q* is chosen to be uniform.

Simulation prototype

The dynamical simulation of a hippocampal network (Extended Data Fig. 3), which was used as a proof of concept, is a simplified version of a previously published in silico model of the human dentate gyrus[100], which has been used to study disease progression in epilepsy[42]. Simulated kalium channelrhodopsin channels[40] were added to a variable fraction of cells within this model to probe the efficacy of optogenetic feedback in disturbing seizure-like events. Excitatory and inhibitory neurons were modeled as point neurons using a simplified dynamical model[104], which was modified to use conductance-based synapses. The network, increased in size from the original to allow seizure-like events to propagate for a longer duration, consisted of 1,000 excitatory GCs and 12 inhibitory BCs evenly spaced on concentric half-circles of radius 800 µm and 750 µm, respectively. Each GC was randomly connected via AMPA synapses to 50 of the 100 nearest GCs as well as the three nearest BCs, and each BC was randomly connected via GABA synapses to 100 of the nearest 140 GCs as well as the two neighboring BCs. All synapses use a conductance whose timecourse follows a difference-of-exponentials form with parameters taken from Buchin et al.[42]. Dynamical parameters of the individual neurons were taken from Izhikevich et al.[104], but the original model does not include a membrane capacitance due to its use of instantaneous synapses, so the membrane capacitance for each cell type was selected to recapitulate the dynamical behavior observed in Buchin et al.[42].

To interrupt the seizure-like synchronization behavior observed in this model, a light-sensitive kalium channelrhodopsin[40] was added to the model. The channel is modeled as being open whenever the light input is active, with its activation decaying exponentially with a time constant of 50 ms, as suggested by Extended Data Fig. 3. The reversal potential is given by Govorunova et al.[40] as −85 mV, and the conductance is set to 20 pS to match the peak current in Extended Data Fig. 3. The channel was enabled in a variable fraction p_{opto} of simulated GCs. Then, during simulations, the optogenetic channel was controlled in closed loop: simulation was performed in 1-ms steps, and, if the total spike count in a single step exceeded a threshold x_{opto}, the optogenetic channel was enabled for a duration T_{opto}.

The first second of each simulation was ignored to allow the network to reach its steady-state behavior. All simulations were implemented using NEST simulator version 3.4 (ref. 105), with models implemented using the modeling language NESTML[106]. Full simulation code, including all parameters used, is available in the GitHub repository 'Simulation' directory at https://github.com/braingeneers/AndrewsGengVoitiukEtAl_SourceCode.

Theta waveform videos

The theta waveform videos (Supplementary Videos 3 and 4) depict how theta phase signals in local field potential propagate through the tissue over time. The video comprises two animated figures. The left figure, explained further below, displays theta signals across all recording electrodes. Theta activity is aligned in time with the neural firing rate, displayed in the right figure. This is done to convey how theta activity is modulated during neural bursts. The moving vertical line in the firing rate figure illustrates the exact timing of the theta waves to the left. The videos move at a pace that is 10 times slower than real time. This is done to better understand the nuances in theta activity during bursts.

The theta wave activity for each electrode was calculated using a standard neuroscience protocol. The raw data for an electrode were normalized and then had a low bandpass filter applied to them. Then, a second bandpass filter was applied to select activity within the theta frequencies, between 4 Hz and 8 Hz.

To express the evolution in theta activity across the roughly 1,000 recording electrodes of the HD-MEA, we use colors and circles of varying sizes. The center of each circle is the position of a single recording electrode. The color of the circle displays whether the theta activity for that particular electrode is in a positive or negative phase (that is, whether the wave is positive or negative at that point in time). The size of the circle displays the relative amplitude of the theta wave (that is, the magnitude of the wave's value at that time). As mentioned in the main text, at times of regular neural activity, the theta waves are roughly randomly distributed, but, during epileptiform bursts, there are strongly coherent propagations of synchronized theta waves.

Reporting summary

Further information on research design is available in the Nature Portfolio Reporting Summary linked to this article.

Data availability

Electrophysiological data will be made available on a DANDI public server at: https://dandiarchive.org/dandiset/001132

Other data that support the findings of this study are available in the GitHub repository: https://github.com/braingeneers/AndrewsGengVoitiukEtAl_SourceCode. Any additional data will be made available by the authors upon reasonable request.

Code availability

An annotated summary of custom code used for this study is available at https://github.com/braingeneers/AndrewsGengVoitiukEtAl_SourceCode. MaxWell software, purchased from MaxWell Biosystems, was used for data collection.

Kilosort2 (ref. 98) was used for electrophysiologic data analysis.

All code will be made available upon reasonable request.

References

98. Pachitariu, M., Steinmetz, N. A., Kadir, S. N., Carandini, M. & Harris, K. D. Fast and accurate spike sorting of high-channel count probes with KiloSort. In *Proc. 30th International Conference on Neural Information Processing Systems (NIPS 16)* (eds Lee, D. D. et al.) 4455–4463 (Curran Associates, 2016).
99. Rossant, C. et al. Spike sorting for large, dense electrode arrays. *Nat. Neurosci.* **19**, 634–641 (2016).
100. Siegle, J. H. et al. Survey of spiking in the mouse visual system reveals functional hierarchy. *Nature* **592**, 86–92 (2021).
101. Hill, D. N., Mehta, S. B. & Kleinfeld, D. Quality metrics to accompany spike sorting of extracellular signals. *J. Neurosci.* **31**, 8699–8705 (2011).
102. Someck, S. et al. Positive and biphasic extracellular waveforms correspond to return currents and axonal spikes. *Commun. Biol.* **6**, 950 (2023).
103. Leland, M., John, H. & James, M. Uniform manifold approximation and projection for dimension reduction. Preprint at https://arxiv.org/abs/1802.03426 (2018).

104. Izhikevich, E. M. Simple model of spiking neurons. *IEEE Trans. Neural Netw.* **14**, 1569–1572 (2003).
105. Spreizer, S. et al. NEST 3.3 (2022); https://juser.fz-juelich.de/record/1007653
106. Linssen, C. et al. NESTML 5.2.0 (2023); https://juser.fz-juelich.de/record/1005203

Acknowledgements

This project was supported by the National Institute of Neurological Disorders and Stroke, National Institutes of Health (NIH), through UCSF grant 5R25NS070680-13 (J.P.A.). Its contents are solely the responsibility of the authors and do not necessarily represent the views of the NIH. This study was also supported by the following NIH awards: Brain Initiative award UF1MH130700 (D.V.S., V.S. and T.J.N.); R01NS123263 (T.J.N.); R01MH120295 (S.R.S.); T32HG012344 (K.V.); and K08NS126573 (C.R.C.). In addition, this study was supported by the National Science Foundation (NSF) under award NSF 2034037 (M.T.), the National Human Genome Research Institute under award RM1HG011543 (M.A.T.E., A.R., A.S., D.S., D.E., D.H., S.S. and M.T.) and grants from the Schmidt Futures Foundation (SF 857) (D.H.), the Weill Neurohub (C.R.C.), U01NS132353 (C.R.C), the Esther A. & Joseph Klingenstein Fund (T.J.N.), the Shurl and Kay Curci Foundation (T.J.N. and C.R.C.) and the Sontag Foundation (T.J.N.) as well as a gift from the William K. Bowes Jr. Foundation. T.J.N. is a New York Stem Cell Foundation Robertson Neuroscience Investigator. J.L.S. was supported by the University of California, Santa Cruz (UCSC) Chancellor's Postdoctoral Fellowship, NIH K12GM139185 (through the National Institute of General Medical Sciences to the UCSC Institute for the Biology of Stem Cells) and LRP0000018281 (National Institute of Child Health and Human Development). Support was also provided by the Citizens United for Research in Epilepsy (CURE) Taking Flight Award (C.R.C). We thank Flaticon for images used to design Fig. 2. We thank the Pacific Research Platform, supported by the NSF under awards CNS-1730158, ACI-1540112, ACI-1541349 and OAC-1826967; the University of California Office of the President; the University of California, San Diego's California Institute for Telecommunications and Information Technology/Qualcomm Institute; as well as the Corporation for Education Network Initiatives in California. The funders had no role in study design, data collection and analysis, decision to publish or preparation of the manuscript. Materials were obtained and supplied by the authors. We would like to acknowledge K. Hengen for feedback in manuscript preparation. We would like to acknowledge the courageous patients who agreed to have their treatments contribute to the advancement of knowledge and science.

Author contributions

J.P.A., J.G. and K.V. contributed equally. J.P.A. conceived the project, obtained tissue, designed experiments, conducted experiments, analyzed the data, interpreted the data, performed histology and wrote the manuscript. J.G. constructed the analysis pipeline, analyzed data, interpreted results, created figures and drafted the manuscript. K.V. built and fabricated the optogenetic slice recording system, wrote the code for integration of the MEA system with optogenetic recordings, conducted experiments, wrote experimental code, created figures and drafted the manuscript. M.A.T.E., D. Shin, A.R. and A.S. also contributed equally. M.A.T.E. conducted experiments, wrote experimental code, designed the closed-loop experiment, analyzed theta wave phase propagation, created theta oscillation videos and created figures. D. Shin designed, tested and optimized the tissue culture pipeline, designed AAV plasmids, assisted in experimental design and provided feedback on manuscript drafting. A.R. designed code for MEA analysis and designed figures. A.S. designed the in silico modeling of hippocampal epileptiform activity, created the in silico modeling figure, designed and implemented the HDBSCAN analyses and created the HDBSCAN analysis figure. Other co-author contributions are as follows. A.W. cultured hippocampal slices and performed and analyzed histology. L.L. consulted on AAV design and edited the manuscript. D. Solis designed theta coherence k-distance analysis, conducted local field potential analyses and assisted with figure design. M.G.K. and J.L.S. contributed to MEA recording and optogenetic experimental design. J.A.R.d.J. transduced tissue and edited the manuscript. K.C.D. performed whole-cell patch clamping and analysis. H.H.L. cultured and processed tissue. D.E. contributed to hardware design and MEA recording techniques. K.I.A. provided mentorship and experimental tissue. S.S., V.S., T.S., D.H., C.R.C. and D.V.S. provided mentorship, intellectual consultation, experimental design input and analytic methods advice and edited the manuscript. E.F.C. provided mentorship, intellectual consultation and human tissue samples and edited the manuscript. M.T. provided mentorship and intellectual consultation, oversaw data analysis and rig fabrication, contributed to experimental design and edited the manuscript. T.J.N. conceived the project, designed experiments, interpreted data and wrote the manuscript.

Competing interests

The authors declare no competing interests.

Additional information

Extended data is available for this paper at https://doi.org/10.1038/s41593-024-01782-5.

Supplementary information The online version contains supplementary material available at https://doi.org/10.1038/s41593-024-01782-5.

Correspondence and requests for materials should be addressed to Edward F. Chang, Mircea Teodorescu or Tomasz Jan Nowakowski.

Peer review information *Nature Neuroscience* thanks the anonymous reviewers for their contribution to the peer review of this work.

https://doi.org/10.1038/s41593-024-01782-5

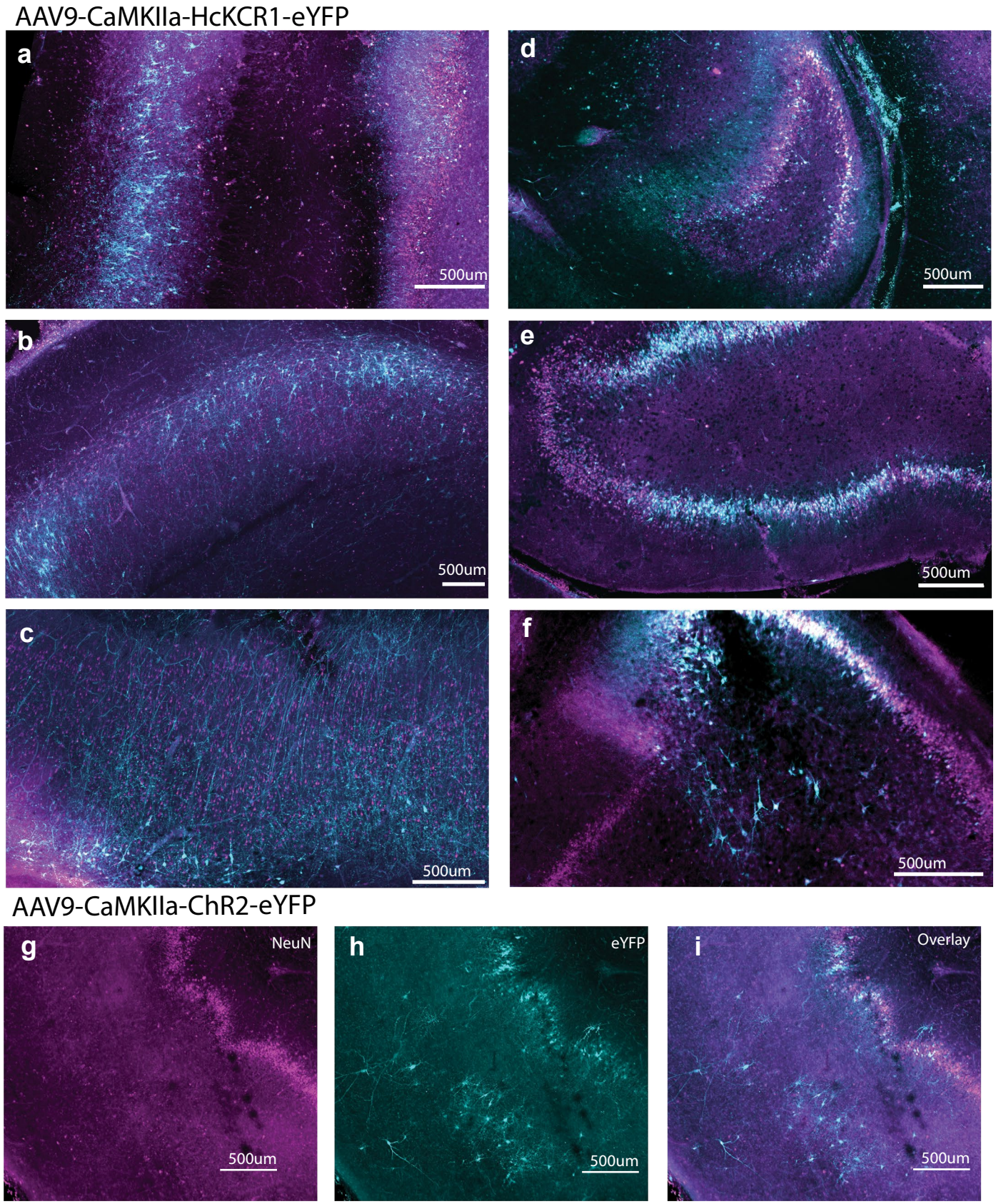

Extended Data Fig. 1 | Slice histology. Representative Immunohistochemistry overlay from 7 of the 12 slices listed in Table 1. **a-f**, hippocampal slices transduced with AAV9-CaMKIIa-HcKCR1-eYFP. **g-i**, 1 of 2 slices transduced with AAV9-CaMKIIa-ChR2-eYFP. Magenta represents NeuN and cyan represents eYFP expression, correlating to neurons that express the HcKCR1-eYFP or ChR2-eYFP construct. **a-c**, Examples of slices where predominately CA regions were recorded. **a**, Slice 3C, **b**, slice 8D, **c**, slice 12G. **d-f**, Examples of slices where predominately granule cell layer (GCL) of the dentate gyrus areas were recorded. **d**, Slice 9E, **e**, slice 10F, and **f**, slice 11G. Scale bars all represent 500 microns. **g-i**, Slice 4C, transduced with AAV9-CaMKIIa-ChR2-eYFP.

https://doi.org/10.1038/s41593-024-01782-5

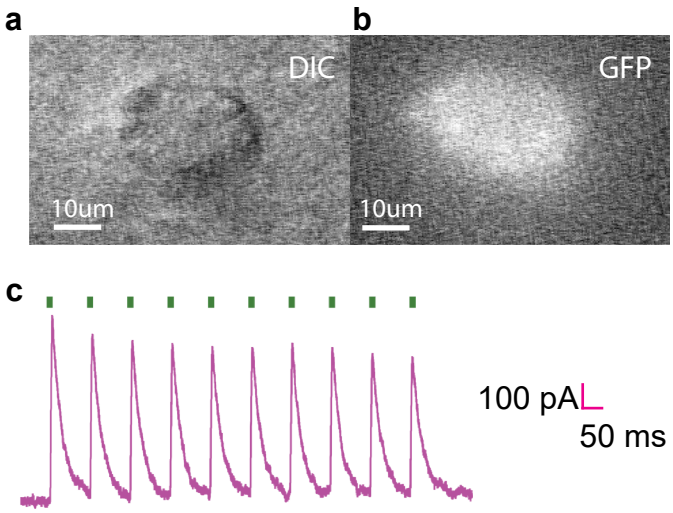

Extended Data Fig. 2 | Patch clamp of HcKCR1. a, DIC microscopic image of a neuron in a hippocampal slice transduced with AAV9-CaMKIIa-HcKCR1-eYFP. **b**, Green fluorescence of the same cell as in **a**, confirming viral transduction. **c**, Voltage clamp recording of the cell above showing hyperpolarizing currents activated with brief pulses of 540nm light illumination, represented by green rectangles above the hyperpolarizing currents elicited by illumination. This was repeated in 3 cells over 2 separate hippocampal slices.

https://doi.org/10.1038/s41593-024-01782-5

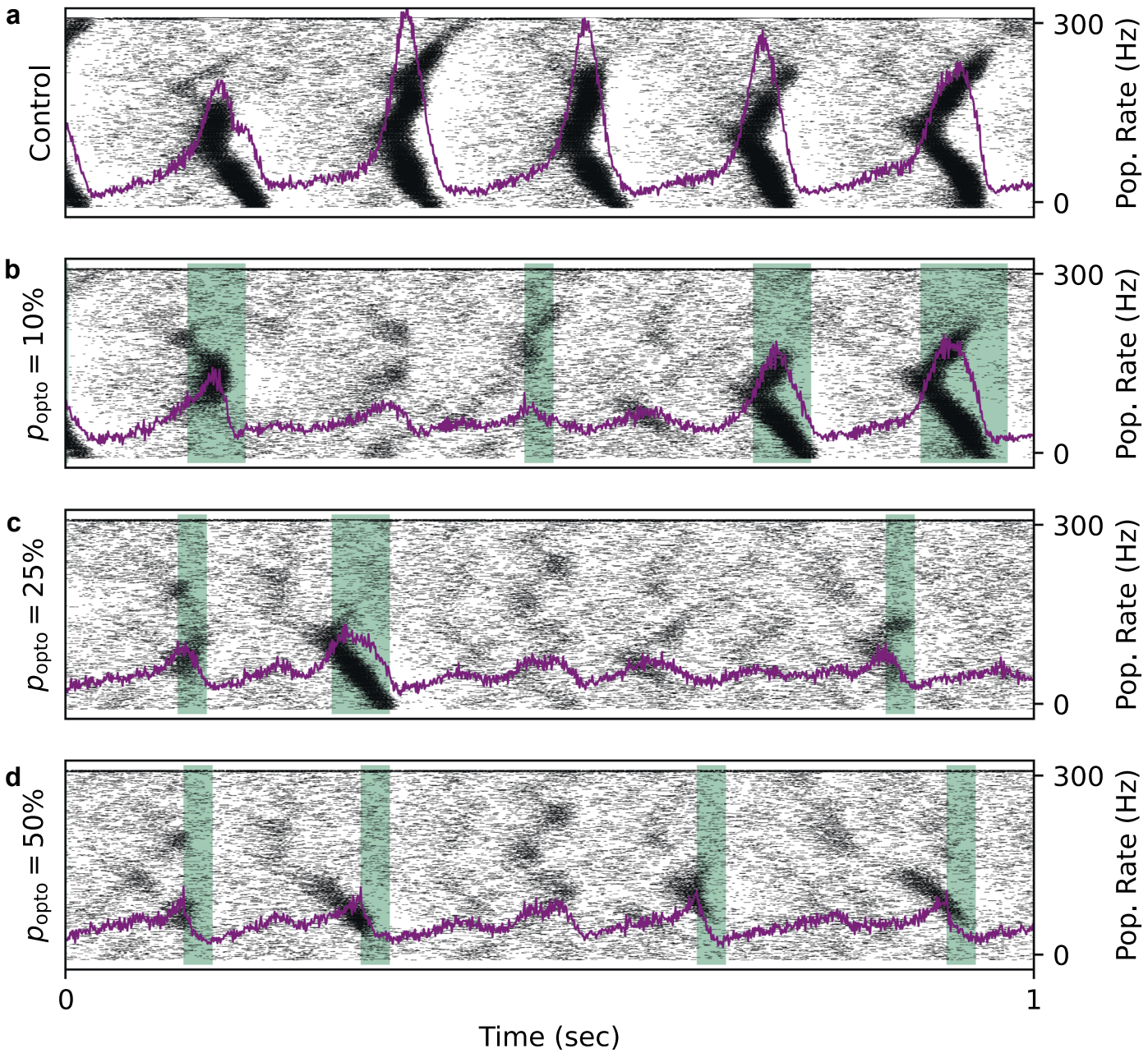

Extended Data Fig. 3 | In silico model. Raster plots of simulated activity of an in silico model of granule and basket cells of the human hippocampus. Each black dot represents a single-unit firing event, so dark areas represent clusters of high firing rates consistent with epileptiform activity. **a**, Examples of spontaneous seizure-like events in presence of no light-responsive cells. A simulated 'light-on' phase is indicated in green. **b-d**, Raster plots of the simulation data with **b**, 10%, **c**, 25% and **d**, 50% of excitatory granule cells harboring an inhibitory, light-sensitive channel.

https://doi.org/10.1038/s41593-024-01782-5

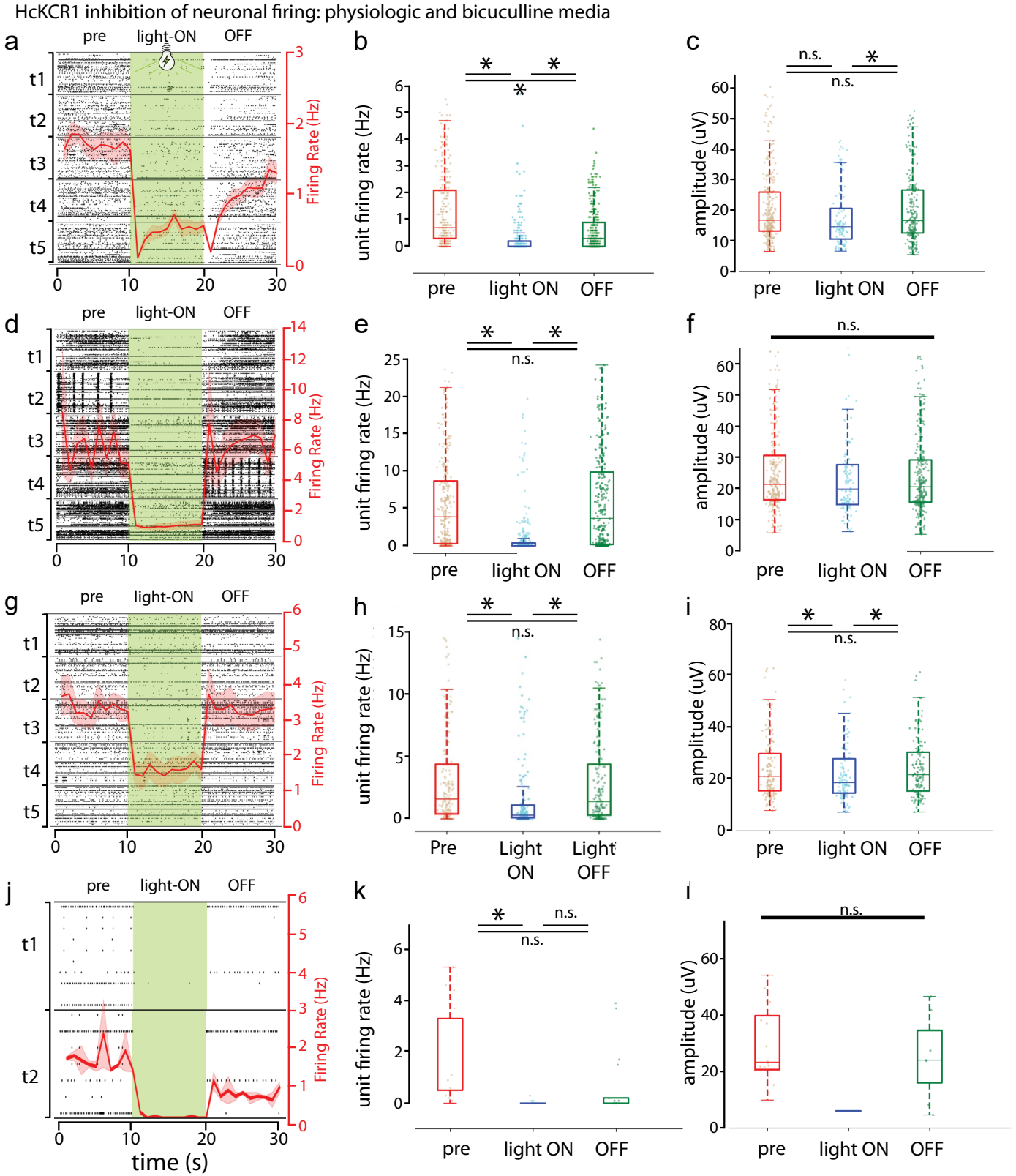

Extended Data Fig. 4 | See next page for caption.

https://doi.org/10.1038/s41593-024-01782-5

Extended Data Fig. 4 | Optogenetic inhibition in physiologic and bicuculline media. a, Stacked raster plots of hippocampal slice 3C ($n = 64$ units) expressing HcKCR1 illuminated with 10s of continuous 530nm LED light. Average firing rate (Hz) is overlaid in red, with shaded red representing standard error of the mean, for multiple trials of 10s of light illumination (green rectangle from 10–20s on stacked raster plots), and paired comparisons of **b**, firing rate and **c**, spike amplitude (uV) for the 10s prior to illumination (pre), during illumination (light ON) and following illumination (OFF). On the y-axis are 5 trials (t1 – t5) of continuous 10s illumination, stacked align the light ON phase (green). **d-f)** Same parameters as shown in **a-c**, are shown for slice 5C ($n = 65$ units), recorded with bicuculline. **g-i**) same parameters for slice 7D ($n = 44$ units), recorded with bicuculline. **j-l**, for slice 8D ($n = 10$ units), recorded with bicuculline. Firing rate and amplitude comparisons were made with a two-tailed paired t-test comparing average firing rates and amplitudes under each condition. See Supplementary Table 4 for *P*-values for each comparison. For all box and whisker plots, the box extends from the first quartile to the third quartile of the data, with a line at the median. The whiskers extend from the box to the farthest data point lying within 1.5x the inter-quartile range from the box. For stacked raster plots (a, d, g, j) the translucent pink color surrounding the firing rate red line represents the standard error of the mean (SEM) for the firing rate. **P*-values were judged to be significant if adjusted *P*-values were less than 0.05. Exact *P*-values reported in Supplementary Table 4.

https://doi.org/10.1038/s41593-024-01782-5

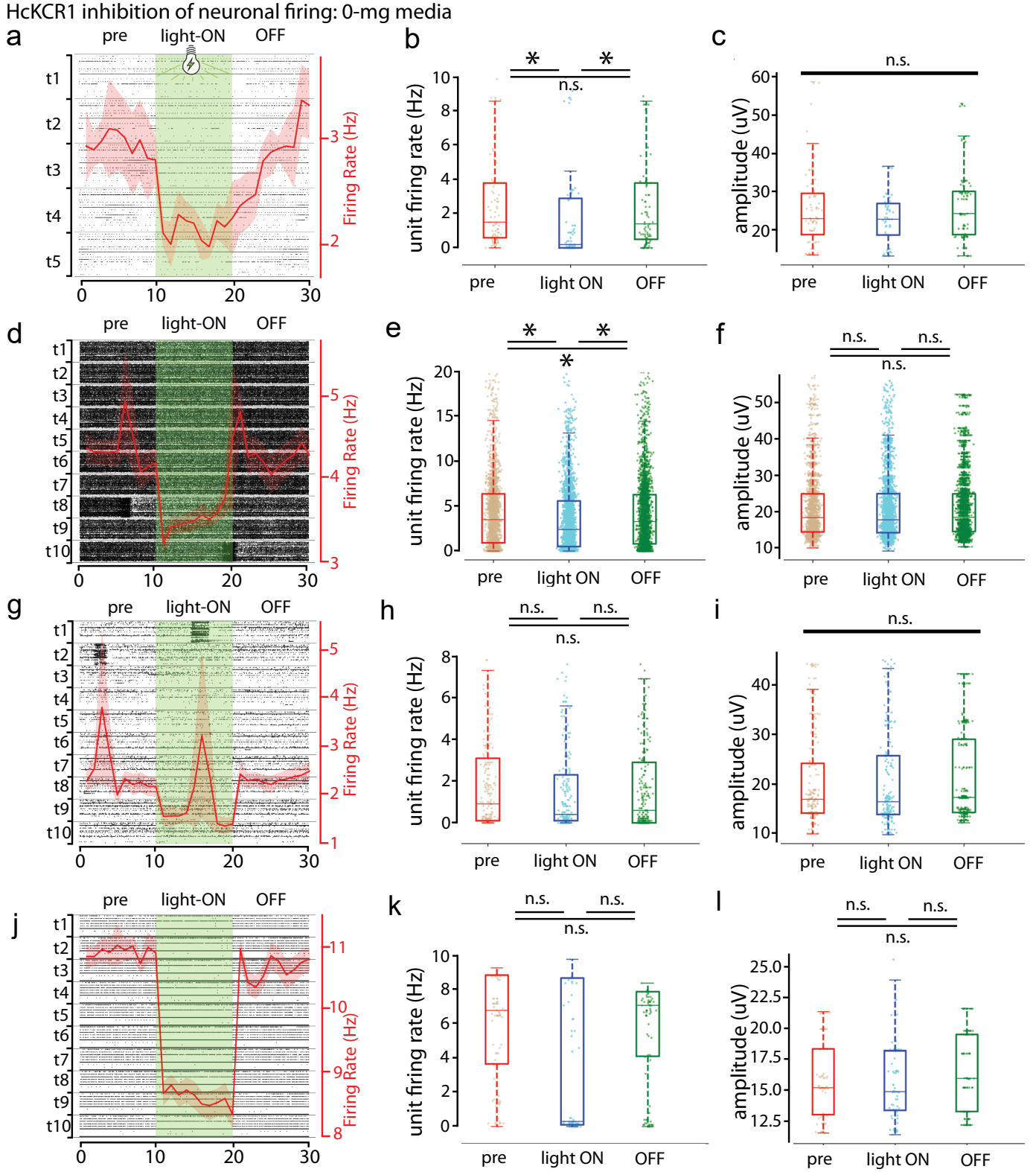

Extended Data Fig. 5 | Optogenetic inhibition in 0-mg media. a, Stacked raster plots from Slice 9E ($n = 17$ units) with average firing rate (Hz) overlaid in red, with shaded red representing standard error of the mean, for multiple trials of 10s of light illumination, and paired comparisons of **b**, firing rate and **c**, spike amplitude for the 10s prior to illumination (pre), during illumination (light ON) and following illumination (OFF). Data shown from 4 slices recorded in 0-mg media. **d**, Raster plot with firing-rate overlay showing isolated bursts of activity in trials T8 and T10 in slice 10F (n = 228 units). **e-f**, firing rate and amplitude data from slice 10F ($n = 228$ units). **g-i**, Slice 11G ($n = 23$ units), showing isolated bursts of activity in trials T1 and T2. **j-l**, Slice 12G ($n = 9$ units). Firing rate and amplitude comparisons were made with a two-tailed paired t-test comparing average firing rates and amplitudes under each condition. See Supplementary Table 5 for *P*-values for each comparison. For all box and whisker plots, the box extends from the first quartile to the third quartile of the data, with a line at the median. The whiskers extend from the box to the farthest data point lying within 1.5x the inter-quartile range from the box. * *P*-values were judged to be significant if adjusted *P*-values were less than 0.05. Exact *P*-values reported in Supplementary Table 5.

https://doi.org/10.1038/s41593-024-01782-5

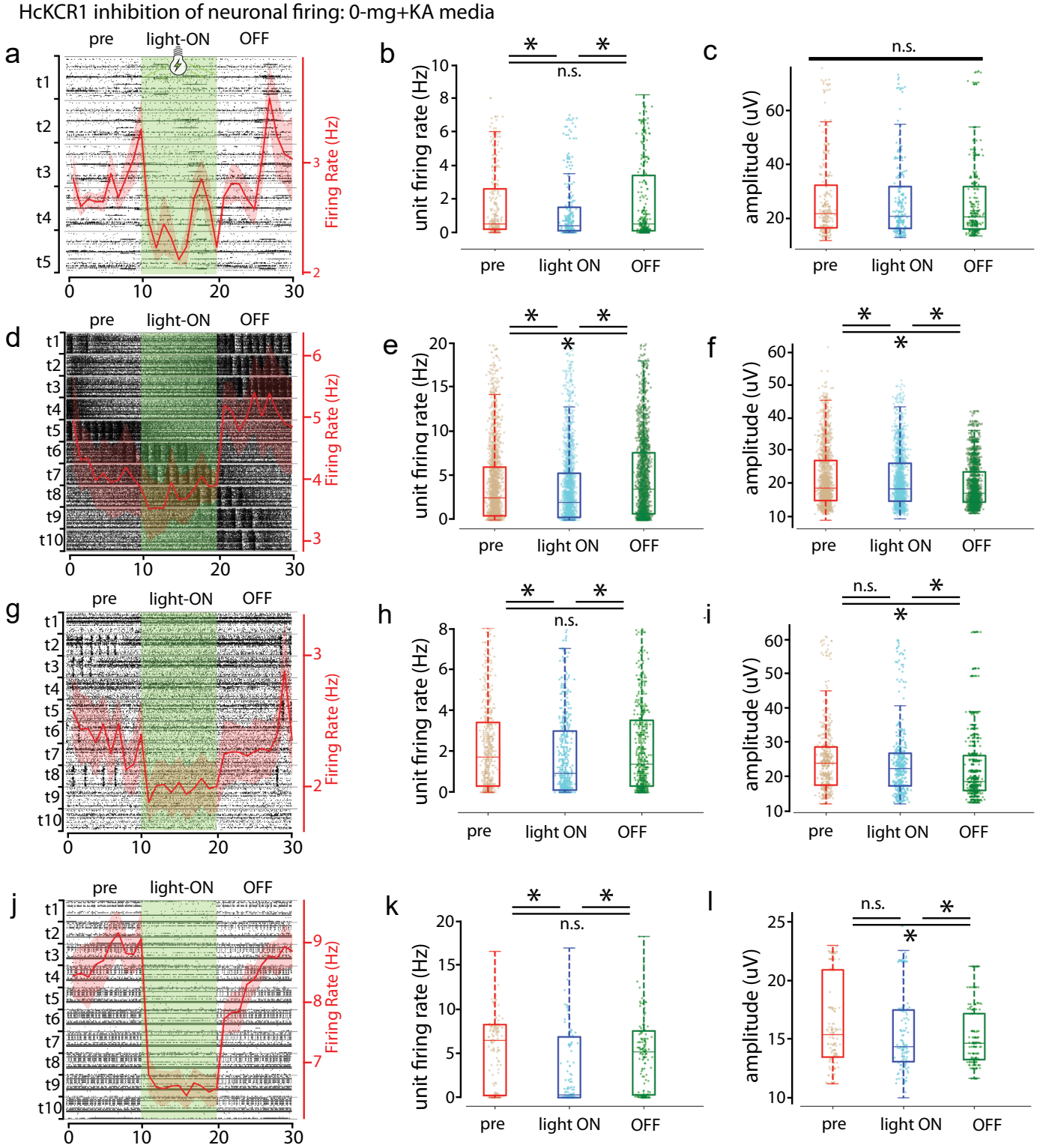

Extended Data Fig. 6 | Optogenetic inhibition in 0-mg + KA media. a, Stacked raster plots of Slice 9E ($n = 57$ units) with average firing rate (Hz) overlaid in red, with shaded red representing standard error of the mean, for multiple trials of 10s of light illumination, and paired comparisons of **b**, firing rate (Hz) and **c**, spike amplitude (uV) for the 10s prior to illumination (pre), during illumination (light ON) and following illumination (OFF). Data shown for 4 slices recorded under 0-mg+KA conditions. **d-f**, data from Slice 10F ($n = 212$ units). **d**, slice 10F exhibits rhythmic burst activity, with persistent bursts of during trials T6-T8. **e-f**, Neuronal firing rate and amplitude. **g-i**, data from slice 11G ($n = 55$ units). **g**, Slice 11G exhibiting clusters of rhythmic burst activity that does not persist during light-ON conditions. **h-i**, Neuronal firing rate and amplitude. **j-l**, data from slice 12G ($n = 17$ units). All slices show reduced firing rates during light-ON conditions. See Supplementary Table 6 for *P*-values for each comparison. For all box and whisker plots, the box extends from the first quartile to the third quartile of the data, with a line at the median. The whiskers extend from the box to the farthest data point lying within 1.5x the inter-quartile range from the box. Firing rate and amplitude comparisons were made with a two-tailed paired t-test comparing average firing rates and amplitudes under each condition. * *P*-values were judged to be significant if adjusted *P*-values were less than 0.05, exact *P*-values reported in Supplementary Table 6.

https://doi.org/10.1038/s41593-024-01782-5

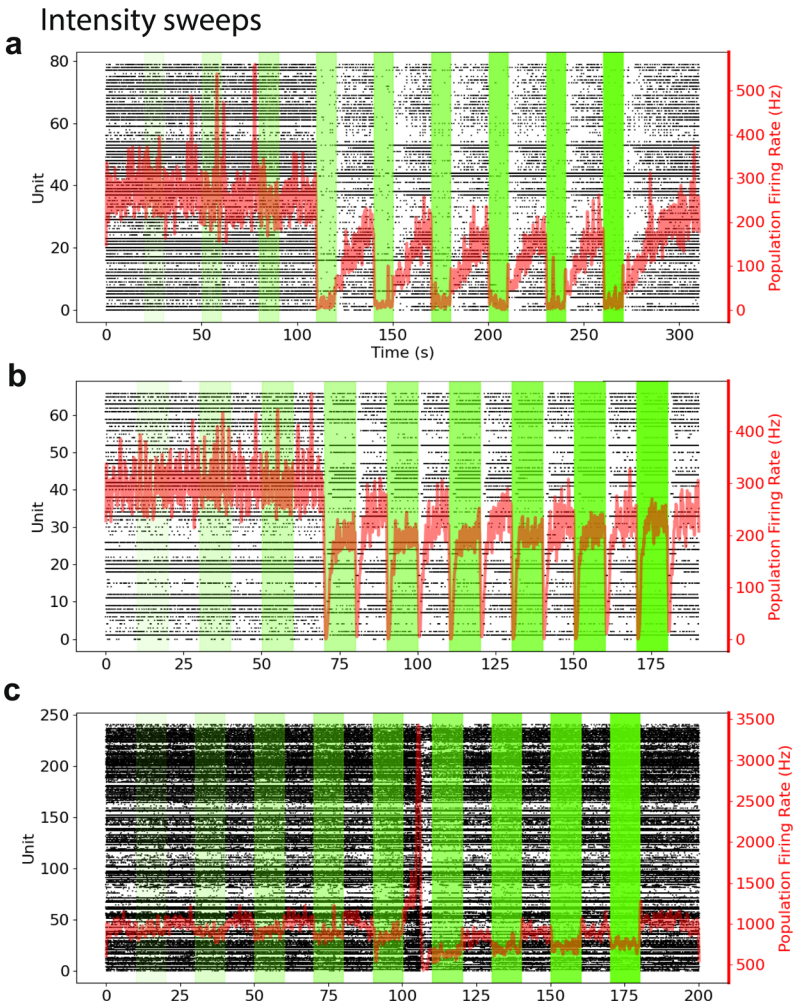

Extended Data Fig. 7 | Intensity sweeps. Unit activity with firing rate overlaid during the intensity sweeps for 3 separate slices. **a**,**b**, Intensity scans of 2 slices (**a** = slice 3C, **b** = slice 5C) recorded in physiologic media, **c**, intensity scan of a slice (**c** = slice 10F) recorded in 0-mg media.

https://doi.org/10.1038/s41593-024-01782-5

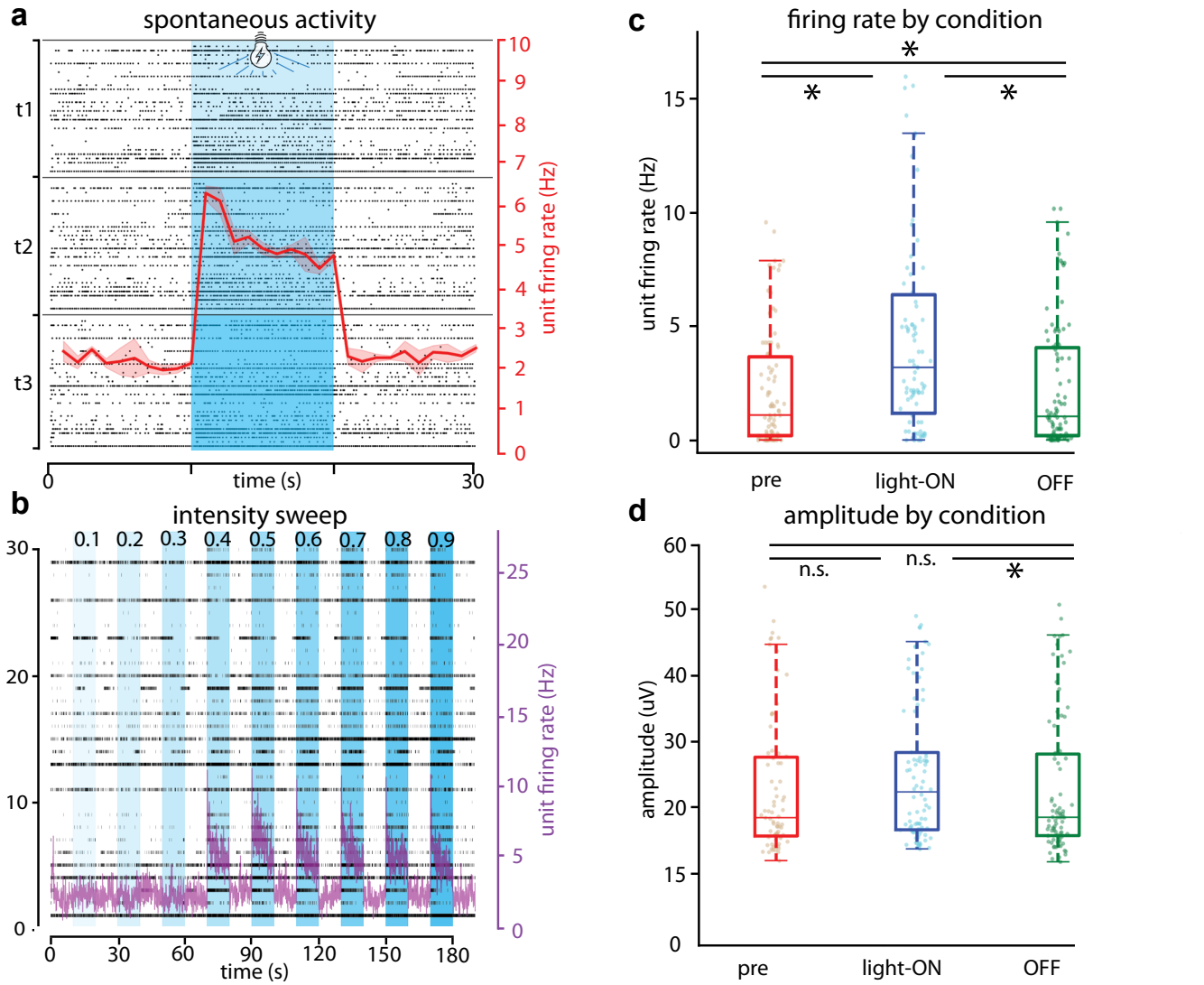

Extended Data Fig. 8 | ChR2 activation. a, Stacked raster plots from slice 4C ($n = 30$ units) with average unit firing rate (Hz) overlaid in red, with shaded red representing standard error of the mean, showing ChR2-mediated increases in firing rate during light-ON conditions. **b**, intensity sweep, **c**, firing rate comparisons and **d**, spike amplitude comparisons for the same slice. Firing rate statistics for a two-tailed paired t-test comparing average firing rates and amplitudes under each condition, $n = 30$ units (c): Pre vs light-ON raw P-value = 3.22E-04, holm-bonferroni adjusted P-value = 0.001. Light-ON vs OFF raw P-value = 7.34E-04, holm-bonferroni adjusted P-value = 0.001. Pre vs OFF raw P-value = 0.106, holm-bonferroni adjusted P-value = 0.106. Amplitude statistics, $n = 30$ units (**d**): Pre vs light-ON raw P-value = 0.127, holm-bonferroni adjusted P-value = 0.254. Light-ON vs OFF raw P-value = 0.027, holm-bonferroni adjusted P-value = 0.082. Pre vs OFF raw P-value = 0.106, holm-bonferroni adjusted P-value = 0.255. For all box and whisker plots, the box extends from the first quartile to the third quartile of the data, with a line at the median. The whiskers extend from the box to the farthest data point lying within 1.5x the inter-quartile range from the box.*comparisons were deemed statistically significant if adjusted P-values were less than $P = 0.05$.

https://doi.org/10.1038/s41593-024-01782-5

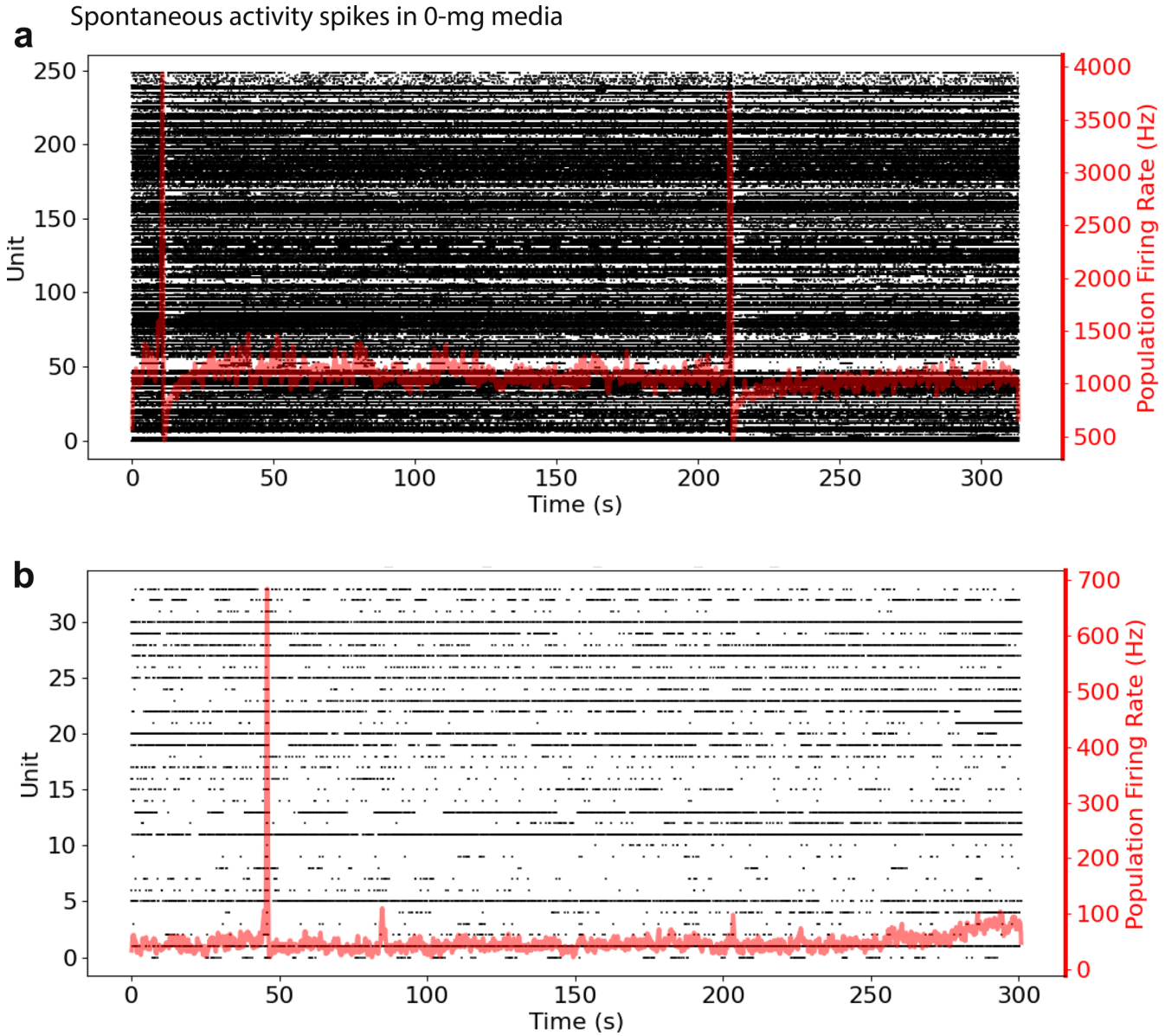

Extended Data Fig. 9 | Zero-Mg spikes. a, Slice 10F and **b**, 9E showing isolated <1s bursts of activity during 5 minutes of continuous recording.

nature portfolio

Corresponding author(s): Edward F. Chang
Mircea Teodorescu
Tomasz Jan Nowakowski

Last updated by author(s): Aug 7, 2024

Reporting Summary

Nature Portfolio wishes to improve the reproducibility of the work that we publish. This form provides structure for consistency and transparency in reporting. For further information on Nature Portfolio policies, see our Editorial Policies and the Editorial Policy Checklist.

Statistics

For all statistical analyses, confirm that the following items are present in the figure legend, table legend, main text, or Methods section.

n/a	Confirmed	
☐	☒	The exact sample size (*n*) for each experimental group/condition, given as a discrete number and unit of measurement
☐	☒	A statement on whether measurements were taken from distinct samples or whether the same sample was measured repeatedly
☐	☒	The statistical test(s) used AND whether they are one- or two-sided *Only common tests should be described solely by name; describe more complex techniques in the Methods section.*
☐	☒	A description of all covariates tested
☐	☒	A description of any assumptions or corrections, such as tests of normality and adjustment for multiple comparisons
☐	☒	A full description of the statistical parameters including central tendency (e.g. means) or other basic estimates (e.g. regression coefficient) AND variation (e.g. standard deviation) or associated estimates of uncertainty (e.g. confidence intervals)
☐	☒	For null hypothesis testing, the test statistic (e.g. *F*, *t*, *r*) with confidence intervals, effect sizes, degrees of freedom and *P* value noted *Give P values as exact values whenever suitable.*
☒	☐	For Bayesian analysis, information on the choice of priors and Markov chain Monte Carlo settings
☒	☐	For hierarchical and complex designs, identification of the appropriate level for tests and full reporting of outcomes
☒	☐	Estimates of effect sizes (e.g. Cohen's *d*, Pearson's *r*), indicating how they were calculated

Our web collection on statistics for biologists contains articles on many of the points above.

Software and code

Policy information about availability of computer code

Data collection	all custom code is available in a public GitHub archive at https://github.com/braingeneers/AndrewsGengVoitiukEtAl_SourceCode and this is mentioned in the Code Availability statement. MaxWell ® software purchased from Maxwell Biosystems (mxwbio.com) was used for HD-MEA data collection
Data analysis	all custom code is available in a public GitHub archive at https://github.com/braingeneers/AndrewsGengVoitiukEtAl_SourceCode and this is mentioned in the Code Availability statement. Kilosort2 was used for electrophysiologic data analysis

For manuscripts utilizing custom algorithms or software that are central to the research but not yet described in published literature, software must be made available to editors and reviewers. We strongly encourage code deposition in a community repository (e.g. GitHub). See the Nature Portfolio guidelines for submitting code & software for further information.

Data

Policy information about availability of data

All manuscripts must include a data availability statement. This statement should provide the following information, where applicable:

- Accession codes, unique identifiers, or web links for publicly available datasets
- A description of any restrictions on data availability
- For clinical datasets or third party data, please ensure that the statement adheres to our policy

Electrophysiological data will be made available on a DANDI public server at:
https://dandiarchive.org/dandiset/001132

Other data that support the findings of this study are available in the GitHub repository https://github.com/braingeneers/AndrewsGengVoitiukEtAl_SourceCode. Any additional data will be made available upon reasonable request from the authors.

Research involving human participants, their data, or biological material

Policy information about studies with human participants or human data. See also policy information about sex, gender (identity/presentation), and sexual orientation and race, ethnicity and racism.

Reporting on sex and gender	See Table 1 for sex and age of patients from whom samples were obtained
Reporting on race, ethnicity, or other socially relevant groupings	Because samples used in the study are de-identified, we do not have information about race, ethnicity or other socially relevant groupings
Population characteristics	Patient age, sex and pathologic diagnosis is provided in Table 1. All patients had refractory epilepsy, which is defined as treatment failure of appropriate trials of 2 or more anti-epileptic drugs
Recruitment	There was no recruitment for this study. Any patients undergoing surgical resections for epilepsy at our institution are offered the opportunity to consent to have resected tissue be utilized for IRB-approved research protocols, namely that under which this study was performed. There is no patient compensation. This could introduce a bias toward populations with access to medical care and health insurance.
Ethics oversight	University of California-San Francisco Institutional Review Board.

Note that full information on the approval of the study protocol must also be provided in the manuscript.

Field-specific reporting

Please select the one below that is the best fit for your research. If you are not sure, read the appropriate sections before making your selection.

☒ Life sciences ☐ Behavioural & social sciences ☐ Ecological, evolutionary & environmental sciences

For a reference copy of the document with all sections, see nature.com/documents/nr-reporting-summary-flat.pdf

Life sciences study design

All studies must disclose on these points even when the disclosure is negative.

Sample size	Sample sizes were maximized based on the availability of human brain tissue samples. There was no randomization. Samples were processed and experiments run in the order that patient tissue became available. No statistical method was used to predetermine sample size, but our sample sizes are similar to those reported in previous publications
Data exclusions	All slices included in electrophysiologic analyses were from adult patients with refractory epilepsy and were cultured for 4-8 days prior to recordings. Acute recordings were excluded from waveform clustering analyses. These were excluded because there are no optogenetic interventions on acute slice samples and they were not transduced with any AAVs, plus they were not cultured. This allows the data analyzed to be from the most homogenous cohort possible without introducing poorly understood variables. Any slice from which unit activity was not recorded after plating on HD-MEAs was not included in electrophysiologic analyses because there was no electrophysiologic data on these slices to analyze. These were decisions made after data collection.
Replication	All information about experimental replicates are explicitly stated in the manuscript Figure legends.
Randomization	Randomization is not relevant to the study, because only one sample is being processed at a time. Data collection was performed by independent experimenters from data analysis.
Blinding	Each slice/patient sample was processed and analyzed in the order it was received. Most analyses require comparisons of time during which

Blinding

LED illumination occurred on slices during electrophysiologic recordings. Thus blinding would not allow for the analyses performed in this study.

Reporting for specific materials, systems and methods

We require information from authors about some types of materials, experimental systems and methods used in many studies. Here, indicate whether each material, system or method listed is relevant to your study. If you are not sure if a list item applies to your research, read the appropriate section before selecting a response.

Materials & experimental systems

n/a	Involved in the study
☐	☒ Antibodies
☒	☐ Eukaryotic cell lines
☒	☐ Palaeontology and archaeology
☒	☐ Animals and other organisms
☒	☐ Clinical data
☒	☐ Dual use research of concern
☒	☐ Plants

Methods

n/a	Involved in the study
☒	☐ ChIP-seq
☒	☐ Flow cytometry
☒	☐ MRI-based neuroimaging

Antibodies

Antibodies used

NeuN: guinea pig anti-NeuN, Millipore, ABN90, dilution 1:1000
eYFP: Chicken anti-GFP antibody, Aves, GFP-1020, dilution 1:1000

Validation

NeuN ABN90: ABN90 is a Guinea Pig polyclonal version of the Anti-NeuN, clone A60 (MAB377), a highly characterized and cited mouse monoclonal antibody that specifically recognizes the DNA-binding, neuron-specific protein NeuN, which is present in most CNS and PNS neuronal cell types of all vertebrates tested. NeuN protein distributions are apparently restricted to neuronal nuclei, perikarya and some proximal neuronal processes in both fetal and adult brain although, some neurons fail to be recognized by NeuN at all ages: INL retinal cells, Cajal-Retzius cells, Purkinje cells, inferior olivary and dentate nucleus neurons, and sympathetic ganglion cells are some examples. Presentation
Guinea pig polyclonal serum containing 0.05% sodium azide.
Specificity
This antibody recognizes the N-terminus of NeuN.
Species Cross-reactivity
Demonstrated to react with Mouse and Rat.
Immunogen
GST-tagged recombinant protein corresponding to mouse NeuN.
Molecular Weight
~48 kDa observed
Method of Purification
Unpurified
Control
Mouse brain E16 tissue lysate
Quality Control Testing
Evaluated by Western Blotting in mouse brain E16 tissue lysate.
Western Blotting Analysis: A 1:4,000 dilution of this antibody detected NeuN in 10 µg of mouse brain E16 tissue lysate.

eYFP GFP-1020: Green Fluorescent Protein (GFP) is a naturally fluorescent protein originally derived from jellyfish. GFP has been engineered to produce a vast number of variously colored mutants, fusion proteins, and biosensors which have become useful and ubiquitous tools in transgenic experiments. Fluorescent proteins enable a wide range of applications where they have functioned as cell lineage tracers, reporters of gene expression, or as a measure of protein-protein interactions.
Format IgY Fraction
Concentration 10 mg/mL
Clonality Polyclonal
Isotype IgY
Applications ELISA, ICC, IHC, WB
Host Species Chicken
Molecular Weight 27 kDa
Antigen Recombinant GFP expressed in Escherichia coli
Antibody Registry ID AB_2307313
Storage Store at -20°C in the dark. Under these conditions, the antibodies should have a shelf life of at least twelve months, provided they remain sterile.
Physical State Liquid
Production Notes Chickens were immunized with purified recombinant green fluorescent protein (GFP) emulsified in Freund's adjuvant. After multiple injections, eggs were collected from the hens, and IgY fractions were prepared from the yolks and then affinity-purified antibodies were prepared using GFP conjugated to an agarose matrix. The final product is a filter-sterilized mixture of both affinity-purified antibodies (30 µg/mL) and purified IgY (10 mg/mL).
Buffer Sodium phosphate (10 mM, pH 7.2) buffered isotonic saline (0.9%, w/v), glycerol (50%, v/v), with sodium azide (0.02%, w/v) as an anti-microbial agent.

Dilution Ranges WB: 1:5000-1:10000
IHC: 1:2000-1:5000
ICC: 1:2000-1:5000
Quality Control Antibodies were analyzed by western blot analysis (1:5000 dilution) and immunohistochemistry (1:500 dilution) using transgenic mice expressing the GFP gene product. Western blots were performed using BlokHen® (Aves Labs) as the blocking reagent, and HRP-labeled goat anti-chicken antibodies (Aves Labs, Cat. #H-1004) as the detection reagent. Immunohistochemistry used tetramethyl rhodamine-labeled anti-chicken IgY.

Plants

Seed stocks	Not applicable
Novel plant genotypes	Not applicable
Authentication	Not applicable